

Fisher Glasses: Tail-Certified Quantum Metrology in Quenched Environments

El Mustapha Mansouri and Keigo Arai*

School of Engineering, Institute of Science Tokyo, Yokohama, Kanagawa, 226-8501, Japan

(Dated: July 2, 2026)

Quantum metrological advantage is certified by averaged Fisher responses: contrast, susceptibility, or quantum Fisher information (QFI). This fails in quenched sensors, where slow environmental variables freeze within a session but vary between repetitions: shallow nitrogen-vacancy (NV) centers, superconducting qubits with slow two-level fluctuators, and semiconductor spin qubits in drifting charge noise. They sample session-resolved Fisher geometries, not an averaged channel. Certification conditions on the latent session, projects nuisance directions, inverts to attainable loss, then tail-certifies; this inverse upper-tail loss defines quenched tail-certified information. A no-go theorem: no averaged Fisher data determine this certificate; ensembles sharing averaged Fisher matrix, QFI, and projected information have finite or zero certified precision. A Fisher-zero integrability transition governs collapse: the inverse-loss tail exponent β sets the boundary, with nonintegrable certified loss for $\beta \leq 1$, even when annealed information is large or scaling. The certified quantum resource is response transverse to latent disorder, not raw amplification sharing its generator; universal design laws: safe windows, nondegenerate portfolios, Fisher reserves, action separation, Fisher-cut criteria. A shallow-NV Ramsey tournament shows average-QFI optimization is tail-catastrophic, whereas tail-certified designs recover nearly three orders of magnitude in certified information at equal shot budget and latent ensemble. These non-self-averaging phases are Fisher glasses, governed by Fisher-zero rare-event statistics.

I. INTRODUCTION: AVERAGE QFI CERTIFIES THE WRONG OBJECT

What does a quantum Fisher information (QFI) certificate certify? In the standard theory it certifies the local distinguishability of a fixed or self-averaged channel: a larger phase shift, susceptibility, contrast, or QFI is read as a larger guaranteed precision [1–3]. Entangled probes, critical sensors, collective spin states, Greenberger–Horne–Zelinger (GHZ) protocols, and hybrid solid-state sensors are all built to amplify the imprint of a target parameter on a quantum state [4–8], and realistic noise is known to modify or destroy ideal quantum-metrological scaling [9–12]. All of this presumes that the experiment actually samples the channel whose QFI is computed.

Many solid-state quantum sensors violate this presumption at the session scale. A shallow nitrogen-vacancy (NV) center near sparse surface spins, a superconducting qubit coupled to individual two-level fluctuators, or a semiconductor spin qubit in a slowly varying charge environment sees a single frozen disorder configuration throughout one calibration-and-sensing session, while nominally identical sessions sample different configurations [13–20]. The experiment is therefore quenched, not annealed: the data in a session are generated by a conditional channel selected by a hidden environmental configuration, not by the averaged channel used in a design calculation. The shallow NV makes the stakes tangible (and becomes a quantitative design tournament in Sec. VIII). The positions and couplings of its surface spins are frozen while the device is calibrated and run;

most freezes are benign, but a rare one places a bath-coherence node inside the chosen interrogation window and erases the usable information for that entire session. A designer who optimizes the average response can fund, build, and deploy a sensor that is certified precise on paper yet operationally useless on exactly the sessions that decide the measurement.

This is the failure of an average taken over the wrong object. Averaging the Fisher response over the latent ensemble is like judging a river safe to cross by its mean depth: the average is reassuring and the arithmetic is exact, but one never crosses at the average. One fords the particular bed one is given, and a single deep stretch (one session in which the usable information collapses) is fatal whatever the benign mean promised. A quantum sensor likewise faces one frozen environment per session and must survive the specific configuration it is dealt, not the ensemble average.

Average QFI therefore answers the wrong operational question. It certifies the distinguishability of an averaged channel, a fiction that no single run ever realizes. A quenched experiment instead asks a sharper question: in the one frozen session that actually occurs, once the slow environmental directions are set aside as nuisance directions, what loss is attainable? This distinction matters because precision is governed by inverse information, so a small set of sessions in which the usable information nearly vanishes can dominate the certified loss even when the average response is large. Certifying the average therefore does not certify the experiment one runs.

The repair is an order-of-operations change, as described by Eq. (1). One must first condition on the frozen session, then project the slow nuisance directions, then invert the remaining information to the attainable loss,

* Corresponding author: arai.k.835f@m.isct.ac.jp

and only then certify its upper tail over future sessions,

$$\xi \longrightarrow J(\xi) \longrightarrow F_{\theta|\mu}(\xi) \longrightarrow \ell(\xi) \longrightarrow \text{CVaR}_\alpha[\ell]. \quad (1)$$

We call the inverse of this upper-tail loss the tail-certified information. When this certificate vanishes while the averaged response remains large, we call the regime a *Fisher glass*. The formal definitions are given in Sec. II. The central claim is that this order cannot be reconstructed after averaging: once the latent-session distribution is compressed to an averaged Fisher matrix or averaged QFI, the tail of the inverse loss has already been erased, and no later certificate can recover it. Figure 1 contrasts the two paradigms.

We develop the certification theory of this quenched Fisher geometry and establish four results. First (Sec. III), averaged Fisher data are insufficient: two latent ensembles can share the same averaged Fisher response yet have different tail-certified precision, including the case of finite precision for one and zero for the other, and the tail-certified risk is in general not even a renormalized Fisher matrix. Second (Sec. IV), the certificate is controlled by the tail of the inverse loss, so a simple Fisher zero already produces a Fisher glass, while higher-codimension failures and nondegenerate portfolios restore integrability. Third (Secs. V–VI), the certified quantum resource is not raw amplification but the component of the signal response transverse to the latent-disorder directions, with a Holevo extension for vector targets. Fourth (Secs. VII–VIII), these principles become concrete design laws (safe interrogation windows, nondegenerate portfolios, configuration-wise Fisher reserves), and a shallow-NV Ramsey tournament shows that the average-QFI optimum can be tail-catastrophic while tail-certified designs recover orders of magnitude in certified information.

Relation to neighboring frameworks. The distinguishing feature is the order forced by frozen latent sessions in Eq. (1): CVaR, nuisance projection, and Fisher zeros become a precision certificate only when composed in this order. Decoherence-limited QFI theory [9–12], fixed-model nuisance metrology [21–23], Bayesian [24, 25] and minimax [26, 27] metrology, and compound/random-channel and finite-sample or outage-style analyses [28] each average, fix, or worst-case the model at an earlier stage; quenched Fisher-glass certification instead treats the projected attainable loss itself as a random variable over frozen session labels and certifies its upper tail. The framework-by-framework comparison is given in the Supplemental Methods (Table III). Throughout, “advantage” refers to the certified local information gain of a quantum-enhanced protocol relative to its chosen benchmark, and this comparison must be made with the quenched tail-certified loss rather than averaged QFI.

II. QUENCHED METROLOGICAL EXPERIMENT

We consider nominally identical estimation sessions performed in a non-self-averaging environment. At the start of session i , a latent environmental configuration ξ_i is sampled from a device/environmental law π_ξ and held fixed through that session’s calibration and sensing shots. The target parameter θ is a deterministic local parameter common to the benchmarked sessions and is *not* assigned a prior; the risk is over future session labels, not over θ . Conditional on ξ_i , data are generated by a local model $\rho_{\theta,\mu}^\xi$, where μ denotes slow nuisance coordinates that affect the record but are not reported targets. Calibration may estimate session-specific contrast, curvature, or a reduced description of ξ_i ; it conditions the estimator on the current session but does not replace the experiment by an annealed channel. Throughout, $\xi \sim \pi_\xi$ is the session-fixed configuration, $J(\xi)$ is the conditional Fisher (or QFI) matrix, scalar and directional Fisher informations are denoted by F with subscripts, and $\ell_{\mathcal{P}}(\xi)$ is the conditional estimation loss of protocol \mathcal{P} .

A. Notation and the quenched certification pipeline

The quenched certification is assembled in the fixed, noncommuting order of Eq. (1): condition on the frozen session ξ , project the nuisance directions, invert to a loss, and only then tail-certify. These operations do not commute because averaging before inversion fundamentally changes the operational precision guarantee. Conditioning fixes $J(\xi)$; projecting the slow coordinate μ leaves the usable scalar information $F_{\theta|\mu}(\xi)$, written $F_\perp(\xi)$ in the general projected case; and inverting gives the session loss $\ell(\xi) = 1/F_{\theta|\mu}(\xi)$. A short scope summary closes this section, with the full assumptions in Table II (Sec. IX).

The averaged response defines the annealed descriptor

$$I_{\text{ann}} = \mathbb{E}_\xi[F_\perp(\xi)], \quad (2)$$

with $\mathbb{E}_\xi \equiv \mathbb{E}_{\xi \sim \pi_\xi}$ the latent-session average; the raw average QFI $\mathbb{E}_\xi[J_{\theta\theta}(\xi)]$ is even less conservative, since $J_{\theta\theta} \geq F_\perp$ pointwise (nuisance projection only removes information). We use “averaged Fisher descriptor” broadly for the QFI $J_{\text{ann}} = J(\bar{\rho}_\theta)$ of the annealed channel $\bar{\rho}_\theta = \mathbb{E}_\xi[\rho_{\theta,\mu}^\xi]$ and for averages of conditional Fisher responses such as $\mathbb{E}_\xi[J_{\theta\theta}(\xi)]$ or $\mathbb{E}_\xi[F_\perp(\xi)]$; none of these determines the quenched inverse-loss tail.

The operational precision certificate is instead defined by the inverse upper-tail risk of the conditional loss,

$$\mathcal{I}_\alpha^{\text{TC}}(\mathcal{P}) := [\text{CVaR}_\alpha(\ell_{\mathcal{P}}(\xi))]^{-1}, \quad 0 \leq \alpha < 1. \quad (3)$$

For scalar or directional targets $\ell_{\mathcal{P}}(\xi) = F_{\theta|\mu,\mathcal{P}}^{-1}(\xi)$; for vector quantum targets the reported target is B_θ and $\ell_{\mathcal{P}}$ is the nuisance-projected Holevo loss $C_{B_\theta|\mu}^H(W_B; \xi)$, with

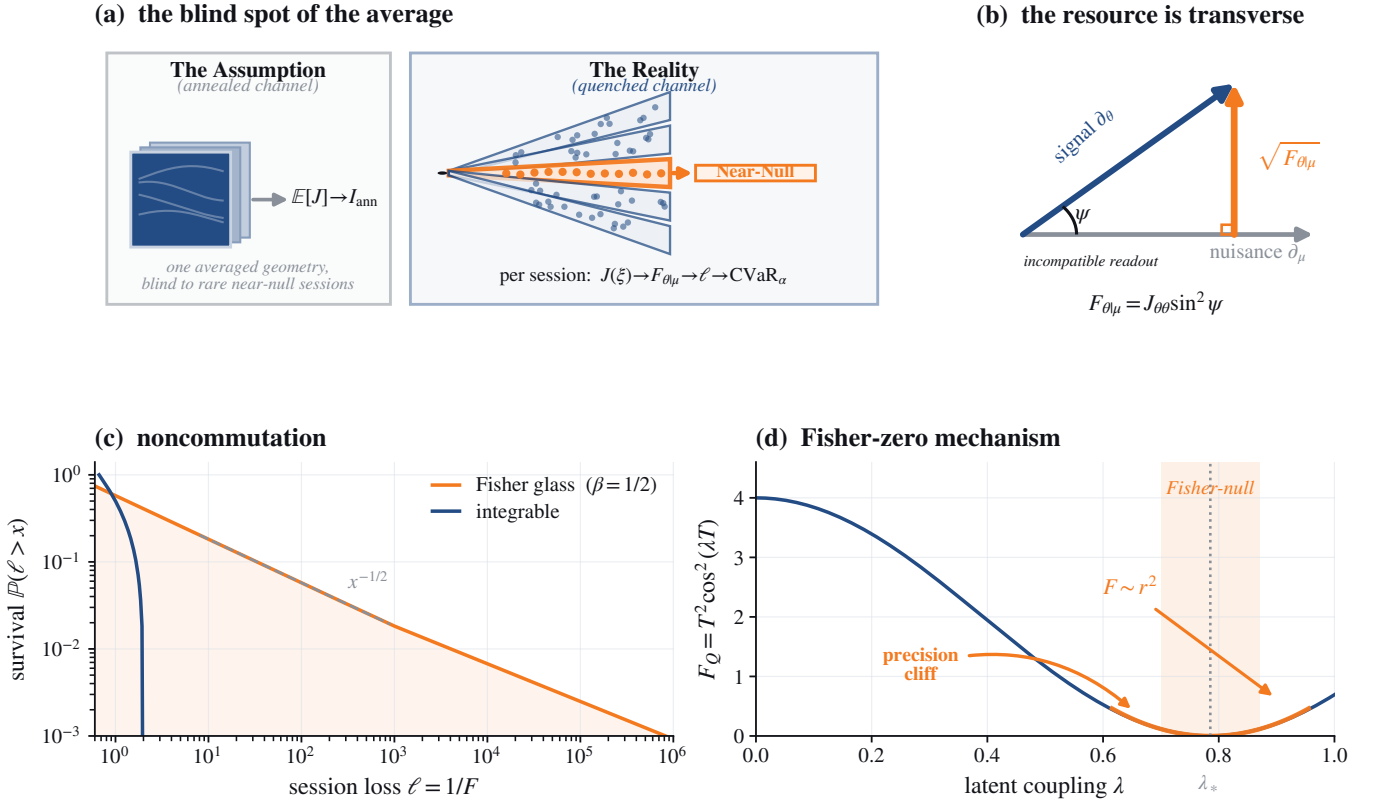


FIG. 1. **Quenched Fisher geometry: a visual abstract.** (a) The averaged-channel paradigm certifies one geometry, $\mathbb{E}[J] \rightarrow$ average QFI, whereas the quenched, non-self-averaging experiment samples a distribution of session-resolved geometries $J(\xi)$, each fed through the noncommuting pipeline $J \rightarrow F_{\theta|\mu} \rightarrow \ell \rightarrow \text{CVaR}_\alpha$ of Eq. (1), so rare near-null sessions ($F_\perp \approx 0$) hidden by the average dominate the loss. (b) The certified resource is the response transverse to the latent nuisance, $F_{\theta|\mu} = J_{\theta\theta} \sin^2 \psi$; for a vector target the obstruction is measurement incompatibility, quantified by the Holevo loss of Sec. V. (c) Two latent ensembles with the same mean $\mathbb{E}[F] = 1$ but different inverse-loss tails, one integrable (finite certificate) and one Fisher-glass ($\beta = 1/2$, $\mathcal{I}_\alpha^{\text{TC}} = 0$), that no averaged Fisher quantity can distinguish. (d) Microscopic mechanism: a simple Fisher zero $F_Q = T^2 \cos^2(\lambda T) \sim r^2$ near a node gives $\mathbb{P}(F_Q^{-1} > x) \sim x^{-1/2}$, the generic nonintegrable Fisher-glass tail.

positive weight W_B on the reported target components, of Sec. V. The conditional value-at-risk $\text{CVaR}_\alpha(X)$ is the mean of the worst $1 - \alpha$ fraction of the loss distribution, a coherent upper-tail risk measure [29–31]; its dual form and the CVaR–QCRB bound are derived in Appendix B. When the CVaR in Eq. (3) is infinite, the certified information is zero. A protocol can therefore have large or scaling I_{ann} yet $\mathcal{I}_\alpha^{\text{TC}} = 0$. This establishes the defining signature of a Fisher glass: quantum enhancement survives in the annealed Fisher geometry while disappearing as an operational quenched resource. The collapse is reached by two mechanisms invisible to the averaged geometry. Either the amplified response aligns with a latent nuisance direction, so signal and environment become locally indistinguishable; or rare configurations make the usable information collapse. The law π_ξ may come from a physical latent-environment model or from the empirical distribution of repeated calibration sessions; for a single slowly drifting device the same certificate is a block-sampled time-series certificate when the drift is stationary or slowly mixing, and otherwise a

finite-catalog empirical certificate.

Core objects and notation. A frozen session label $\xi \sim \pi_\xi$ fixes the conditional Fisher matrix $J(\xi)$; nuisance projection gives the usable scalar information $F_\perp(\xi) = F_{\theta|\mu}(\xi)$, the loss $\ell(\xi) = 1/F_\perp(\xi)$, and, for an estimation protocol \mathcal{P} with loss $\ell_{\mathcal{P}}$, the certificate $\mathcal{I}_\alpha^{\text{TC}}(\mathcal{P}) = [\text{CVaR}_\alpha(\ell_{\mathcal{P}}(\xi))]^{-1}$ of Eq. (3). Every later object specializes this pipeline.

The pointwise quantum Cramér–Rao bound (QCRB) is the operational bridge from information to loss. For a locally unbiased scalar estimator with conditional mean-square loss $R(\xi; \theta)$ and n independent shots, monotonicity of CVaR applied to the pointwise bound $R(\xi; \theta) \geq 1/[nF_Q(\theta, \xi)]$, with $F_Q(\theta, \xi)$ the session-conditional scalar QFI, gives

$$\text{CVaR}_\alpha(R(\xi; \theta)) \geq \text{CVaR}_\alpha\left(\frac{1}{nF_Q(\theta, \xi)}\right). \quad (4)$$

Thus a protocol with large average QFI has zero tail-certified information whenever $\text{CVaR}_\alpha(1/F_Q) = +\infty$.

When the inverse-loss survival function obeys

$$\mathbb{P}(\ell_{\mathcal{P}} > x) \sim A_{\beta} x^{-\beta}, \quad 0 < A_{\beta} < \infty, \quad (5)$$

finite certified information is equivalent to $\beta > 1$. The confidence level α is a reporting choice; the tail-integrability boundary $\beta = 1$ is not, because if the inverse-loss mean is nonintegrable then every finite-level upper-tail CVaR is infinite in the ideal latent distribution. The multiparameter, directional, and Holevo versions of Eq. (4), together with the CVaR preliminaries, are collected in the Supplemental Methods (Appendix B). The remaining sections identify the operational loss $\ell_{\mathcal{P}}$ and the physical mechanisms that set β .

Scope of the main statements (full assumptions in Table II).

Result	Main assumption
CVaR-QCRB certificate	session-fixed latent ξ ; local regularity
Geometric Fisher-zero exponent	smooth latent density; local zero $F \sim r^{2m}$ (vanishing order m)
Portfolio law $x^{-K/2}$ (K arms)	independent, zero-nondegenerate arms
Shallow-NV tournament	sparse quasi-static random-telegraph-noise (RTN) model

III. NO-GO THEOREM FOR ANNEALED CERTIFICATION

The conceptual core of the theory is a no-go statement: the quenched certificate is not a functional of the averaged Fisher geometry. This is stronger than saying average QFI is loose; it says average QFI discards information that decides whether the certificate is finite at all. The following theorem shows that no quantity derived from the averaged Fisher geometry can serve as an operational precision certificate in a quenched experiment.

Theorem 1 (No averaged Fisher certification). *There exist latent-session ensembles with the same averaged Fisher matrix $\bar{J} = \mathbb{E}_{\xi}[J(\xi)]$ and the same averaged projected information $\mathbb{E}_{\xi}[F_{\theta|\mu}(\xi)]$, but different tail-certified information*

$$\mathcal{I}_{\alpha,\theta|\mu}^{\text{TC}} = \left[\text{CVaR}_{\alpha} \left(F_{\theta|\mu}^{-1}(\xi) \right) \right]^{-1}, \quad (6)$$

including one with $\mathcal{I}_{\alpha,\theta|\mu}^{\text{TC}} > 0$ and one with $\mathcal{I}_{\alpha,\theta|\mu}^{\text{TC}} = 0$. Consequently, operational certification is encoded in the quenched inverse-loss statistics rather than in any averaged Fisher geometry.

It suffices to treat the scalar case and embed it as the θ block of a larger Fisher matrix. One ensemble has $F(\xi) = 1$ deterministically, so $\text{CVaR}_{\alpha}(F^{-1}) = 1$ and the certificate is finite. The other is chosen with bounded support, density nonzero near $F = 0$ so that F^{-1} has a nonintegrable upper tail, and compensating mass at

larger finite F so that $\mathbb{E}F = 1$. The two ensembles share the averaged Fisher matrix and the average projected information, yet the CVaR of F^{-1} is finite for the first and infinite for the second. Latent certification therefore depends on the projected inverse-loss tail, not on the averaged geometry. The explicit construction is given in Appendix C. Panel 1(c) shows the two ensembles; they are indistinguishable to any averaged Fisher quantity.

A. Breakdown of Fisher geometry

The failure is not repaired by replacing J with some effective J_{eff} . Consider the tail-certified directional risk for target direction w (with $J(\xi)^{-1}$ read as the Moore–Penrose inverse $J(\xi)^+$ on singular strata, as in Appendix B),

$$R_{\alpha}(w) = \text{CVaR}_{\alpha}(w^{\top} J(\xi)^{-1} w). \quad (7)$$

By CVaR duality, R_{α} is a supremum of positive quadratic forms, hence convex and homogeneous of degree two in w , so its unit sublevel set is a symmetric convex *risk body* (Appendix B). But it is in general not quadratic. For two equally likely configurations with $J_1^{-1} = \text{diag}(1, 100)$ and $J_2^{-1} = \text{diag}(100, 1)$ at $\alpha = 1/2$,

$$R_{1/2}(w) = \max\{w^{\top} J_1^{-1} w, w^{\top} J_2^{-1} w\}, \quad (8)$$

which violates the parallelogram identity and therefore cannot arise from any single matrix. In ordinary local metrology a Fisher matrix defines an ellipsoid of distinguishability; in the quenched tail-certified theory the risk body is a convex body that is generally not an ellipsoid. Tail certification is thus not a renormalized QFI but a genuinely different information geometry, which is the precise sense in which the quenched Fisher geometry is a new object.

IV. FISHER-GLASS TRANSITION: THE FISHER-ZERO EXPONENT

Theorem 1 says the certificate lives in the inverse-loss tail; the next result says exactly when that tail is integrable. A *Fisher zero* is any latent configuration where the scalar, directional, or nuisance-projected Fisher information vanishes, whether from bath coherence nodes, channel failure, or loss of transverse identifiability when the signal response becomes tangent to a latent-disorder direction.

The exponent β is the inverse-loss tail index of the quenched experiment. It is not an averaged Fisher quantity: it is defined only after conditioning on the frozen session, projecting nuisance directions, and inverting to the attainable loss. Operationally, β is the certification exponent: $\beta > 1$ gives a finite tail-certified information, while $\beta \leq 1$ is the Fisher-glass regime. Geometrically, Fisher-zero mechanisms set β through codimension and

vanishing order; experimentally, β is the slope measured from session-loss tails.

Theorem 2 (Fisher-glass transition). *Let $F_{\perp}(\xi)$ be the session-resolved projected Fisher information. If, near a Fisher-null set,*

$$\mathbb{P}(F_{\perp} < \varepsilon) \sim A_{\beta} \varepsilon^{\beta}, \quad 0 < A_{\beta} < \infty, \quad (9)$$

then

$$\mathbb{P}(F_{\perp}^{-1} > x) \sim A_{\beta} x^{-\beta}, \quad (10)$$

so $\mathcal{I}_{\alpha}^{\text{TC}} = 0$ for $\beta \leq 1$, even when $I_{\text{ann}} = \mathbb{E}_{\xi}[F_{\perp}(\xi)]$ is large or scaling. More generally, if the Fisher-null set is a smooth codimension- c manifold and, in normal distance r , $F_{\perp} \sim r^{2m}$ and the latent density $p_{\xi} \sim r^{\nu}$, then $\mathbb{P}(F_{\perp}^{-1} > x) \sim A_{\eta} x^{-\eta}$ with the geometric Fisher-zero exponent

$$\eta = \frac{c + \nu}{2m}, \quad (11)$$

so that $\beta = \eta$ when the tail is produced by a geometric Fisher zero, and finite certification requires $\eta > 1$.

Physics behind the theorem. The mechanism is elementary. Let a latent coordinate r measure distance from a simple Fisher zero. Generically $F_{\perp}(r) \simeq a_{\star} r^2$. If sessions sample r with smooth nonzero density at the zero, then

$$\mathbb{P}(F_{\perp} < \varepsilon) = \mathbb{P}\left(|r| < \sqrt{\varepsilon/a_{\star}}\right) \propto \sqrt{\varepsilon}, \quad (12)$$

hence $\mathbb{P}(F_{\perp}^{-1} > x) \propto x^{-1/2}$. Because

$$\mathbb{E}[F_{\perp}^{-1}] = \int_0^{\infty} \mathbb{P}(F_{\perp}^{-1} > x) dx \quad (13)$$

diverges for tail index $\beta \leq 1$, the upper-tail mean loss diverges: a single simple zero in the latent support is already catastrophic.

Why an average response is dangerous. The annealed descriptor $\mathbb{E}[F]$ is insensitive to the integrability of $1/F$, which is exactly the quantity the tail certificate measures. Two protocols with the same $\mathbb{E}[F]$ can sit on opposite sides of the $\beta = 1$ boundary.

This is the whole physical content of the transition: a codimension-one simple zero ($c = 1$, $m = 1$, $\nu = 0$) gives $\eta = 1/2$, while increasing the codimension of simultaneous failure moves η across the tail-integrability boundary $\eta = 1$. The geometric proof is in Appendix G.

These same tail indices double as an experimental diagnostic and preview the repairs of Sec. VII, as the next proposition records.

Proposition 1 (Design principles for escaping the Fisher glass). *Fisher zeros and weakest Fisher cuts set the inverse-loss tail index, while safe windows, nondegenerate portfolios, and Fisher reserves change it in directly measurable ways. The signatures are tail indices: $\beta = 1/2$ ($x^{-1/2}$) for a single unsafe zero, $\beta = K/2$ ($x^{-K/2}$) for a zero-nondegenerate K -arm portfolio, and a safe Fisher reserve changes the universality class by eliminating the algebraic tail altogether.*

Fisher-zero universality. Many microscopic noise models produce the same certification exponent β . In pure-dephasing sensors, real zeros of the bath characteristic function or Loschmidt amplitude are a microscopic source of Fisher zeros [32–35]. If the coherence has first real zero u_1 and the disorder action A (the evolution time setting the accrued latent phase $A\lambda$) satisfies $A\lambda \geq u_1$ (with Λ the maximum latent coupling), neighborhoods of the zero generate the same algebraic inverse-loss tail; for quasi-static two-state noise $u_1 = \pi/2$ (Appendix H). For Ramsey magnetometry at the optimal working point the conditional QFI is $F_Q(T, \xi) = T^2 \mathcal{W}^2(T, \xi)$, with \mathcal{W} the coherence selected by the latent configuration. In the quasi-static two-state limit $W_{\text{RTN}} = \cos(\lambda T)$, so an unsafe single Ramsey arm has the generic $x^{-1/2}$ inverse-Fisher tail. With γ_{RTN} the random-telegraph-noise switching rate, the exact safety boundary is

$$T_{\text{safe}}(\Lambda, \gamma_{\text{RTN}}) = \frac{\pi/2 + \arcsin(\gamma_{\text{RTN}}/\Lambda)}{\sqrt{\Lambda^2 - \gamma_{\text{RTN}}^2}} \quad (14)$$

(Appendix J). For uniform couplings and sparse Poisson fluctuators, $T < T_{\text{safe}}$ keeps the Fisher zero outside the latent support, whereas $T \geq T_{\text{safe}}$ gives infinite CVaR of $1/F_Q$ for every $\alpha < 1$. With Gaussian background contrast of envelope time T_2^* and mean fluctuator number N_f , the conventional average-QFI Ramsey optimum is $T_{\text{avg}} = T_2^*/\sqrt{2} + O(N_f)$ (maximizing $T^2 e^{-2(T/T_2^*)^2}$), and in the tail-catastrophic regime used below the tail-certified (CVaR-optimal) interrogation time T_{TC} satisfies

$$T_{\text{TC}} < T_{\text{safe}} < T_{\text{avg}}. \quad (15)$$

The usual Ramsey design can therefore be average-optimal and tail-catastrophic at once.

Operational regulators in finite data. Real experiments have finite data, bounded estimators, calibration floors, and priors, so every empirical CVaR is finite. This finiteness is not a loophole in the criterion but a regime the theory predicts quantitatively: each regulator converts the sharp $\beta = 1$ transition into a finite precision cap that an experimentalist can compute in advance from the calibration budget.

Finite-data regulators are predictive engineering laws. A hard loss cap ℓ_{max} , additive Fisher floor ε , or finite latent catalog N_{eff} caps the certified information at a value fixed by the regulator: $\mathcal{I}_{\alpha, \ell_{\text{max}}}^{\text{TC}} \propto \ell_{\text{max}}^{-(1-\beta)}$, $\mathcal{I}_{\alpha, \varepsilon}^{\text{TC}} \propto \varepsilon^{1-\beta}$, and $\mathcal{I}_{\alpha, N}^{\text{TC}} \asymp A N_{\text{eff}}^{-(1-\beta)/\beta}$ (with logarithmic forms at $\beta = 1$). Read forward, these regulator-flow laws predict where a design's certified precision plateaus for given hardware; read backward, they size the calibration catalog or loss cap needed to reach a target certificate.

A certificate that still moves with its regulator is not yet intrinsic: regulator-independent certification requires either $\beta > 1$ or a physical Fisher reserve with $F_{\perp}(\xi) \geq F_0 > 0$. Used deliberately, however, the regulator flow is itself a quantitative design tool, proved in Appendix R.

V. THE CERTIFIED QUANTUM RESOURCE IS TRANSVERSE

The quenched certificate changes the meaning of quantum enhancement under latent disorder. The relevant question is not whether the signal susceptibility is large, but whether it remains identifiable after slow environmental directions are projected out.

A. Transverse resource: the physical picture

Before the matrix statement, the mechanism is worth seeing physically. The obstruction appears whenever the target and the latent disorder are written into the probe through a shared generator. This is the situation of trying to hear one tone over a second, nearly identical tone: turning up the volume (raw amplification) boosts signal and background together and leaves them exactly as hard to tell apart. Gain along the shared direction buys no distinguishability; what is needed is a different direction, a component of the response that the disorder does not also produce.

Geometrically, collect the slow latent directions into a nuisance tangent space and picture it as a plane, on which the target imprints a response vector. If that vector lies in the plane, no amount of gain separates signal from environment: its length can grow without bound while its projection onto the orthogonal complement stays zero. Certifiable information is carried only by the part of the response transverse to the plane, which for a single nuisance direction is measured by the *Fisher angle* ψ between the signal response and that direction. As $\psi \rightarrow 0$ the response folds into the nuisance plane and the certified information vanishes no matter how large the raw susceptibility. The Schur-complement algebra of Appendix F is precisely the projection that extracts this transverse component for any number of nuisance directions, and for one it collapses to the one-line law $F_{\theta|\mu} = J_{\theta\theta} \sin^2 \psi$.

B. Scalar nuisance projection

Theorem 3 (The quantum resource is transverse). *Promote a slow latent coordinate to a session-fixed nuisance parameter μ , and let θ be the target. On a regular stratum where the nuisance block is nonsingular, projecting the nuisance out of the session QFI matrix $J(\xi)$ leaves the nuisance-projected Fisher information $F_{\theta|\mu}$, the Schur complement of the nuisance block, whose general form and multi-channel geometry are derived in Appendix F. For a single nuisance coordinate it collapses to the one-line law*

$$F_{\theta|\mu} = J_{\theta\theta} \sin^2 \psi, \quad (16)$$

where the Fisher angle ψ is defined by $\cos \psi = J_{\theta\mu}/(J_{\theta\theta}J_{\mu\mu})^{1/2}$. The operational inverse-Fisher loss for

estimating θ while μ is unknown is $F_{\theta|\mu}^{-1}$, and the certified scalar information in the presence of the nuisance is

$$\mathcal{I}_{\alpha,\theta|\mu}^{\text{TC}} = \left[\text{CVaR}_{\alpha} \left(F_{\theta|\mu}^{-1} \right) \right]^{-1}. \quad (17)$$

The projection must be applied session by session, before inversion and tail certification; otherwise the averaged Fisher geometry hides nonintegrable rare-session losses. Equation (16) makes the obstruction explicit: a divergent scalar QFI does not certify enhancement if the Fisher angle to the nuisance direction closes. The certified resource is not the raw susceptibility $J_{\theta\theta}$ but the susceptibility transverse to the latent-disorder tangent space. The same identifiability principle extends to multi-channel sensors: if all active channels respond to signal and disorder in the same ratio, the target is locally indistinguishable from a nuisance displacement and the projected information vanishes (Sec. VII and Appendix F) [36–38].

Raw amplification that shares a generator with the disorder is not a tail-certified resource. Gain applied along the signal–disorder common direction raises $J_{\theta\theta}$ and the latent-disorder response in the same ratio, leaving the Fisher angle ψ (and hence the certified transverse information $J_{\theta\theta} \sin^2 \psi$) unchanged. Certified enhancement requires increasing the response transverse to the disorder, not the raw susceptibility.

C. Vector targets and the Holevo loss

Measurement incompatibility. The scalar inverse-Fisher loss is only the compatible-measurement limit of the theory. Before the formalism, the geometric picture extends to several targets at once. Where a scalar target was a single response vector poking out of the nuisance plane at angle ψ , a vector target is a rigid bundle of response vectors (a multidimensional shape) protruding from that same plane, and two obstructions now compound. Each component still loses whatever part of its response lies in the nuisance plane; but in addition the components cannot all be read out optimally at once, because the single measurement setting that best resolves one component is not the setting that best resolves another, and these optimal settings are mutually exclusive. This obstruction is the non-commutativity of the per-target optimal measurements; unlike a classical shortfall it is not removed by more signal, and persists at any amplification. The certified loss is then the minimum total unavoidable blur over the bundle, weighted by the importance W_B assigned to each component, namely the volume of the protruding shape that survives both the nuisance projection and this measurement trade-off. The Holevo loss below is the quantitative form of exactly this picture, and raw amplification that merely enlarges the shape inside the nuisance plane does not reduce the blur. In a genuinely quantum multiparameter problem

one specifies the reported target as

$$\vartheta = B\theta, \quad B \in \mathbb{R}^{d_B \times p}, \quad (18)$$

with B full row rank and positive weight $W_B \succ 0$, and replaces $F_{\theta|\mu}^{-1}$ by the attainable nuisance-projected Holevo loss $C_{B\theta|\mu}^H(W_B; \xi)$. The certificate is then

$$\mathcal{I}_{\alpha, B|\mu}^{\text{TC,H}}(W_B) = \left[\text{CVaR}_\alpha \left(C_{B\theta|\mu}^H(W_B; \xi) \right) \right]^{-1}. \quad (19)$$

Tail certification is applied to this session-resolved attainable loss, not to the symmetric-logarithmic-derivative (SLD) Fisher matrix, so the vector Fisher-glass criterion is the tail integrability of $C_{B\theta|\mu}^H$. A minimal pure-qubit example in Appendix D shows that the target map B distinguishes an unidentifiable full target from an identifiable reported component: when an unknown nuisance shifts one quadrature, the full two-parameter target becomes unidentifiable ($C_{\theta|\mu}^H = \infty$) while a reported transverse direction remains finite. Scalar, directional, and full-vector estimation are the cases $d_B = 1$, $B = w^\top$, and $B = I_p$ [21, 39–41].

Quantum attainable loss and measurement incompatibility. The session-resolved loss is a *quantum attainable loss* (the QCRB for scalar targets and the Holevo loss for incompatible multiparameter targets), so measurement incompatibility enters through $C_{B\theta|\mu}^H \geq \text{tr}[W_B B J_{\theta|\mu}^+ B^\top]$, and the certified object is a quenched quantum information geometry, not classical post-processing of an externally given Fisher number. The interpretation of quantum enhancement mechanisms changes accordingly: GHZ, collective, critical [42–46], and error-corrected [47–50] amplification certify only through their Fisher-transverse component g_\perp , not through raw gain g_s (Sec. VI).

VI. ACTION SEPARATION AND TAIL-SAFE QUANTUM ENHANCEMENT

Applying the transverse projection of Theorem 3 to a family of amplified protocols turns the certificate into a scaling law: amplification helps only when it raises the identifiable transverse response faster than the latent-disorder response. Let g_s be the raw signal action gain and g_d the disorder action gain, and define the transverse gain g_\perp by

$$g_\perp^2 T^2 \equiv F_{\theta|\mu}^{\text{amp}}, \quad g_\perp^2 = g_s^2 \sin^2 \psi \quad (20)$$

up to smooth contrast and dimensionless safe-phase factors. At fixed tail-safe latent phase, the per-shot tail-certified information is controlled by

$$\boxed{\mathcal{I}_{\alpha, \text{shot}}^{\text{TC}} \propto \left(\frac{g_\perp}{g_d} \right)^2}, \quad (21)$$

not by g_s^2 . This is the transverse signal–disorder action-separation law (Fig. 2, Appendix I).

The interpretation is immediate. If signal and latent disorder share a common generator, $g_s = g_d = M$, then whenever a latent Fisher zero is present the tail-safe interrogation time must shrink as $T = O(1/M)$ to stay before the zero. This cancels the nominal M^2 per-shot gain: the optimized certified per-shot information is $O(1)$, up to contrast factors (Fig. 2(c)); separating the disorder action from the signal instead restores the M^2 gain (Fig. 2(d)). Common-generator GHZ, collective, and critical amplification are therefore *not* tail-certified resources by themselves; scalable certified enhancement requires $g_\perp/g_d \rightarrow \infty$, a Fisher reserve, or physical removal of the zero. This is the metrological counterpart of the known impossibility of Heisenberg-limited sensing with simply entangled probes in a generic open environment [9–11]. For a critical-sensor family of size L with $g_\perp \sim L^{y_\perp}$ and $g_d \sim L^{y_d}$, the scaling $\mathcal{I}_{\alpha, \text{shot}}^{\text{TC}}(L) \sim L^{2(y_\perp - y_d)}$ [51, 52], together with network, echo, and DC specializations, is given in Appendix F.

VII. TAIL ENGINEERING

Because the certificate is set by the inverse-loss tail, the designs are geometric: they reshape that tail before inversion. There are two kinds. *Intrinsic* repairs change the conditional Fisher geometry $F_\perp(\xi)$ and can produce regulator-independent certification; *extrinsic* regularizers only cap or floor the reported loss and obey the regulator-flow laws of Sec. IV. The intrinsic repairs realize the three slopes of Proposition 1. Each repair below is stated as a transformation of the inverse-loss tail and paired with its consequence on the shallow-NV apparatus of Sec. VIII, whose tournament certifies all four designs at a common shot budget and latent ensemble against the average-QFI baseline.

Safe window. Choose interrogation times before the first latent Fisher zero. In the single-arm Ramsey model this is $T < T_{\text{safe}}$, and the optimum is the CVaR-optimal time inside that window. On the NV magnetometer this single relocation of the working point (from the average-QFI time, which sits beyond the boundary T_{safe} , to a CVaR-optimal time inside the safe window) lifts the certified information by more than three orders of magnitude (Sec. VIII).

Nondegenerate portfolios. Use K active interrogation times with positive shot allocations. If the arms are zero-nondegenerate (no latent configuration kills all arms simultaneously at codimension one), then $\mathbb{P}(\ell_{\text{port}} > x) = x^{-K/2+o(1)}$. Hence $K = 1$ is catastrophic, $K = 2$ is marginal in the regular case, and $K \geq 3$ gives finite CVaR (Appendix M). This threshold is concrete rather than abstract: a three-arm NV portfolio raises the inverse-loss tail index across the $\beta = 1$ boundary and certifies almost three orders of magnitude above the average-QFI design at the identical shot budget (Sec. VIII, Fig. 4(d)).

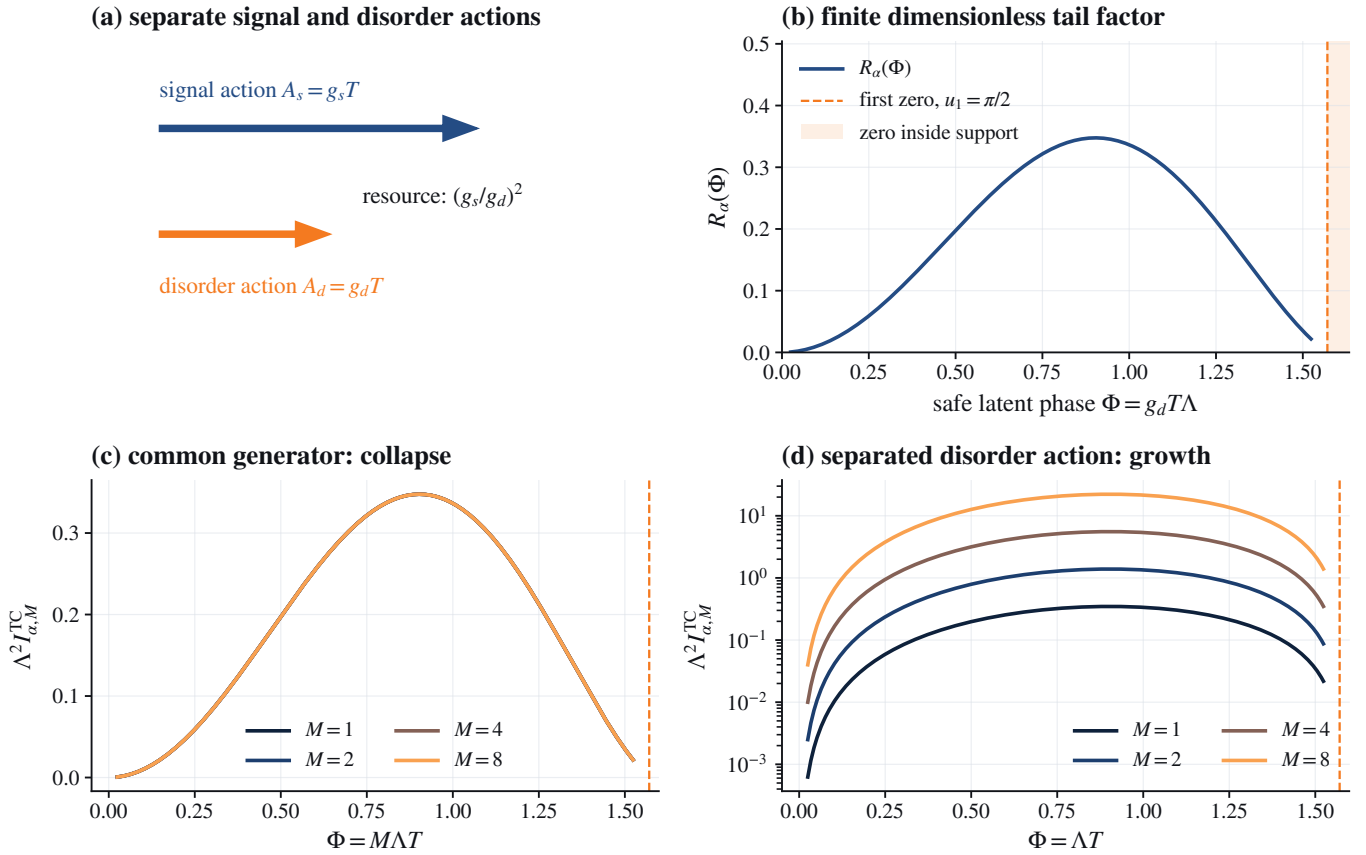


FIG. 2. **Signal–disorder action separation.** Tail-certified amplification is controlled by the ratio of transverse signal action to disorder action. (a) A protocol writes signal and latent disorder into the probe with generally different action gains g_s and g_d ; the fixed-safe-phase resource is $(g_s/g_d)^2$, which becomes $(g_\perp/g_d)^2$ after nuisance projection. (b) Dimensionless tail factor $\mathcal{R}_\alpha(\Phi)$, with Φ the dimensionless safe latent phase, for a two-state Loschmidt response, with first zero at $u_1 = \pi/2$; the certified information vanishes once the latent support reaches the zero. (c) Common-generator amplification, $g_s = g_d = M$ and $\Phi = M \Lambda T$, collapses $\Lambda^2 \mathcal{I}_{\alpha, M}^{\text{TC}}$ for different M . (d) Separated disorder action, $g_s = M$ and $g_d = 1$, gives $\Lambda^2 \mathcal{I}_{\alpha, M}^{\text{TC}} = M^2 \mathcal{R}_\alpha(\Phi)$, restoring scalable per-shot tail-certified gain. In the full multiparameter setting g_s is replaced by the nuisance-projected transverse gain $g_\perp = g_s \sin \psi$.

Fisher reserve. Unlike the previous two strategies, Fisher reserves eliminate the Fisher-zero tail altogether rather than merely changing its exponent. Add a certified safe reference channel with positive shot allocation. If $F_{\text{tot}}(\xi) \geq F_0(\xi) > 0$ for every finite latent configuration, the algebraic Fisher-zero tail is removed; in the sparse Poisson model the remaining tail is super-polynomial (Appendix N). On the optical table this inequality is the literal addition of a short, zero-free anchor arm: the NV reserve design of Sec. VIII bolts a safe reference channel onto the same apparatus, certifying roughly three orders of magnitude above average QFI, while still retaining the long, nominally optimal arm.

Control and encoding. Control, echo, decoherence-free design [53–56], and error-corrected sensing restore certification when they reduce the latent-disorder action, rotate the signal response away from the disorder tangent space, or add a configuration-wise reserve. Same-axis DC sensing is more constrained, because control that cancels quasi-static latent phase also reduces signal area, so uni-

versal scalar tail safety there requires portfolios, reserves, or signal–disorder separation (Appendices O and P).

These rules generalize beyond Ramsey arms through a single architecture law. In a multi-channel sensor one writes the conditional Fisher geometry as a positive sum of channel contributions, $J_{\theta|\mu}(\xi) = \sum_e g_e(\xi) a_e a_e^\top$ with a_e the response direction of channel e , and a *target-identifying Fisher cut* is a set of channels whose simultaneous failure makes the reported target absorbable into the nuisance span. In complex sensing architectures, Fisher zeros are no longer isolated points but propagate through sensing networks, so the relevant object is the weakest Fisher cut.

Theorem 4 (Minimum-cut law for Fisher glasses). *For a positive-channel decomposition of the conditional Fisher matrix with independent channel weights g_e satisfying $\mathbb{P}(g_e < \varepsilon) = \varepsilon^{\eta_e + o(1)}$, the nuisance-projected inverse-loss exponent is set by the weakest target-identifying Fisher*

cut,

$$\mathbb{P}(F_{\theta|\mu}^{-1} > x) = x^{-\beta_{\theta|\mu} + o(1)}, \quad \beta_{\theta|\mu} = \min_{C \in \mathcal{C}_{\theta|\mu}} \sum_{e \in C} \eta_e, \quad (22)$$

where $\mathcal{C}_{\theta|\mu}$ are the cuts after which every remaining channel's target response is absorbable into the nuisance span. Finite tail-certified information requires $\beta_{\theta|\mu} > 1$.

Theorem 4 generalizes the Fisher-zero exponent from isolated zeros to arbitrary sensing architectures. The architecture, not the averaged Fisher matrix, decides the bad-tail exponent: for K generic channels and q nuisance directions with identical simple-zero statistics $\eta_e = 1/2$, the smallest cut has size $K - q$ (the q nuisance directions absorb the target response of at most q channels, so the remaining $K - q$ must fail together), hence $\beta_{\theta|\mu} = (K - q)/2$ and finite certification requires $K \geq q + 3$. The scalar case $q = 0$ recovers the portfolio threshold $K \geq 3$; one nuisance direction raises it to $K \geq 4$. The proof and its graph-Laplacian (Fisher-percolation) specialization are in Appendices E and F. Figure 3 (left) shows the four design classes as distinct survival slopes.

VIII. SHALLOW-NV RAMSEY DESIGN TOURNAMENT

We close with a design tournament in which the standard design rule selects the wrong protocol. A shallow nitrogen-vacancy (NV) center is used as a Ramsey magnetometer in the presence of sparse, slow surface fluctuators [13, 57–61]. This is not an additional assumption of the theory: each session samples a fixed local environment while nominally identical sessions sample different surface-fluctuator configurations, so the NV center is a platform-level instantiation of the conditional Fisher geometry developed above. The simulation gives all quantities in physical units, includes finite readout contrast, and implements an explicit measurement and maximum-likelihood estimator (MLE), not only an information bound. The parameters in Table I are deliberately representative: they stress-test the theory in a zero-crossing regime where the Fisher-null mechanism is active, rather than forecasting one particular device.

The model parameters are listed in Table I: N_f is the mean number of active surface fluctuators, Λ the latent-coupling cutoff, T_2^* the Gaussian Ramsey envelope time, c_{ro} the readout contrast, and $\theta = \gamma_e B_{\text{sig}}$ the target phase per unit time. For session i , a fixed latent configuration is drawn as

$$\xi_i = \{\lambda_{ij}\}_{j=1}^{N_i}, \quad N_i \sim \text{Poisson}(N_f), \quad \lambda_{ij} \sim p_\Lambda, \quad (23)$$

with p_Λ uniform on $[0, \Lambda]$. The Ramsey contrast at interrogation time T is

$$C_i(T) = \exp[-(T/T_2^*)^2] \prod_{j=1}^{N_i} \cos(\lambda_{ij}T), \quad (24)$$

in the quasi-static two-state limit, and the photon-count readout is the Bernoulli channel

$$p_i(1|\theta, T, \varphi) = \frac{1}{2}[1 + c_{\text{ro}}C_i(T) \cos(\theta T + \varphi)], \quad (25)$$

with $\theta = \gamma_e B_{\text{sig}}$ and optimal sensing phase $\varphi = \pi/2$. We compare four protocols at the same total shot budget: the *average-QFI* design uses the time T_{avg} maximizing the latent average of $F_Q(T, \xi)$; the *safe-window* design uses $T_{\text{TC}} < T_{\text{safe}}$ maximizing the empirical certificate; the *portfolio* uses three times $\{1.85, 2.20, 2.65\} \mu\text{s}$; and the *reserve* uses a safe anchor plus a long arm, $\{1.00 \mu\text{s}, T_{\text{avg}}\}$. We run the full six-step tail-certification protocol on the apparatus; the average-QFI design and the three tail-certified designs pass through identical machinery and differ only in their interrogation schedule.

Certification protocol. (i) draw the frozen latent sessions; (ii) estimate the conditional Fisher and loss from a calibration block; (iii) tail-certify via the empirical CVaR; (iv) estimate the inverse-loss tail index against $\beta = 1$; (v) locate the safe transverse geometry; and (vi) validate attainability with an explicit MLE.

Average response and session loss (i)–(ii). The conventional descriptor is computed first: maximizing the latent average QFI $\mathbb{E}_\xi[F_Q(T, \xi)]$ over interrogation time selects the standard Ramsey working point, here the longer $T_{\text{avg}} = 2.11 \mu\text{s}$. For each of the $N_{\text{sess}} = 32000$ sessions a frozen configuration ξ_i of Eq. (23) is drawn (a sparse set of slow surface spins whose quasi-static fields are the magnetic noise the diamond sees on that run), and a calibration block at phases $\varphi = 0, \pi$ estimates the session contrast $\widehat{C}_i(T_k)$ and hence the conditional Fisher estimate

$$\widehat{F}_i(T_k) = \kappa_{\text{ro}} T_k^2 \widehat{C}_i^2(T_k), \quad \kappa_{\text{ro}} = c_{\text{ro}}^2, \quad (26)$$

with κ_{ro} the readout Fisher efficiency, giving the session loss sample $\widehat{\ell}_i = 1/\widehat{F}_i$, or $1/\widehat{F}_{\theta|\mu, i}$ when a nuisance is fitted explicitly (the nuisance-projected Holevo loss $C_{B\theta|\mu}^H$ of Sec. V for a vector target). Sensing shots at $\varphi = \pi/2$ are estimated by MLE, replaced by the profile estimator (covariance governed by $F_{\theta|\mu}^{-1}$) when the nuisance is profiled out.

Tail certification, and the ranking reverses (iii). The session losses are tail-certified,

$$\widehat{\mathcal{I}}_\alpha^{\text{TC}} = \left[\widehat{\text{CVaR}}_\alpha \left(\{\widehat{\ell}_i\} \right) \right]^{-1}, \quad (27)$$

with, for sorted losses,

$$\widehat{\text{CVaR}}_\alpha = \frac{1}{N_{\text{sess}} - k_\alpha} \sum_{j=k_\alpha+1}^{N_{\text{sess}}} \widehat{\ell}_{(j)}, \quad k_\alpha = \lfloor \alpha N_{\text{sess}} \rfloor, \quad (28)$$

and the ranking reverses. At $\alpha = 0.95$ the empirical tail-certified information is 4.15×10^{-6} for the average-QFI design, against 1.27×10^{-2} , 3.88×10^{-3} , and 6.27×10^{-3} for the safe-window, portfolio, and reserve designs, a recovery of roughly 9.4×10^2 to 3.1×10^3 at the same

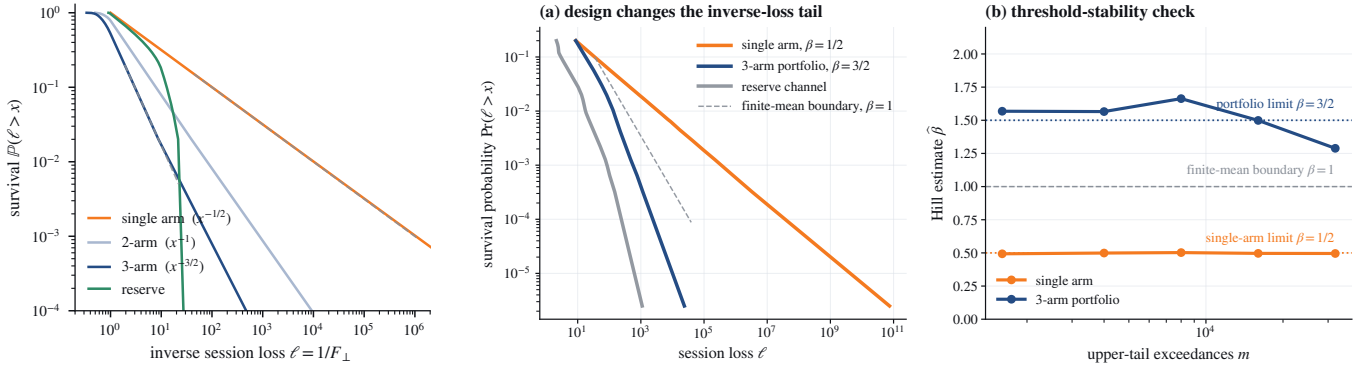


FIG. 3. **Tail diagnostics from session losses.** *Left:* survival functions of the inverse session loss $\ell = 1/F_{\perp}$ for the four design classes: a single unsafe arm follows the nonintegrable $x^{-1/2}$ law (below the finite-mean boundary $\beta = 1$), a two-arm portfolio is marginal (x^{-1}), a zero-nondegenerate three-arm portfolio steepens to $x^{-3/2}$, and a configuration-wise Fisher reserve removes the algebraic zero tail; the measured slope is the inverse-loss tail index β . *Right:* experimental certification from calibrated session losses: (a) survival curves distinguishing unsafe, portfolio, and reserve designs, and (b) Hill upper-tail estimates of β giving a finite-sample stability check against the $\beta = 1$ boundary.

Quantity	Value used	Calibration source	Certificate role
γ_e	$0.176 \text{ rad } \mu\text{s}^{-1} \mu\text{T}^{-1}$	spin resonance	$B_{\text{sig}} \mapsto \theta = \gamma_e B_{\text{sig}}$
c_{ro}	0.18	optically detected magnetic resonance (ODMR)/readout	readout contrast amplitude
T_2^*	$3.0 \mu\text{s}$	Ramsey envelope	background contrast
Λ	$1.0 \text{ rad } \mu\text{s}^{-1}$	noise spectroscopy	$T_{\text{safe}} = \pi/(2\Lambda)$
γ_{RTN}	0	quasi-static limit	separates RTN rate from γ_e
N_f	0.10	session contrast statistics	bad-session probability
N_{sess}	32000	experimental repetitions	latent-environment samples
n	2000	sensing shot budget	estimator variance
R_{err}	8	simulated sensing repeats	Fig. 4(c) MLE-error validation
R_{rob}	16	simulated sensing repeats	supplemental MLE robustness check
n_{cal}	4000	calibration block	curvature uncertainty
θ_0	0	chosen working point	local Ramsey slope
seed	20260430	supplementary code	base random seed

TABLE I. Platform-level parameters for the shallow-NV Ramsey simulation. The values define a representative stress-test point rather than a device-specific fit. Supplemental sensitivity sweeps vary the fluctuator density, dimensionless coupling range, CVaR level, readout contrast, calibration shots, and wall-clock/dead-time budget around this point; supplemental robustness checks test finite-session convergence, seed-to-seed variation, tail-exponent uncertainty, and direct MLE-error validation. At the baseline $\alpha = 0.95$ and $N_{\text{sess}} = 32000$, the empirical CVaR is set by 1600 tail sessions. The estimator-error validation in Fig. 4(c) uses $R_{\text{err}} = 8$ sensing repeats, while the supplemental direct MLE robustness check uses $R_{\text{rob}} = 16$ repeats per calibrated latent session. In an experiment these inputs are obtained from ODMR, Ramsey, echo, and noise-spectroscopy calibration.

shot budget and latent ensemble. The same calibration data that make the average-QFI Ramsey design look optimal expose it as operationally worst once the latent environment is treated as quenched. Session-bootstrap 90% intervals for $\mathcal{I}_{0.95}^{\text{TC}}$ are $[1.89 \times 10^{-6}, 1.74 \times 10^{-5}]$, $[1.24 \times 10^{-2}, 1.29 \times 10^{-2}]$, $[3.56 \times 10^{-3}, 4.27 \times 10^{-3}]$, and $[6.08 \times 10^{-3}, 6.47 \times 10^{-3}]$; the $\alpha = 0.95$ CVaR averages the 1600 worst tail sessions.

Tail exponent and safe geometry (iv)–(v). A finite empirical CVaR is reported with the inverse-loss tail index that produced it. For a threshold u with $m = \#\{i : \hat{\ell}_i >$

$u\}$ exceedances, the Hill diagnostic [62–64]

$$\hat{\beta}(u) = \left[\frac{1}{m} \sum_{\hat{\ell}_i > u} \log \left(\frac{\hat{\ell}_i}{u} \right) \right]^{-1}, \quad (29)$$

with ideal standard error $\hat{\beta}/\sqrt{m}$, places each design relative to $\beta = 1$ (Fig. 3, right); the value is intrinsic only when the lower one-sided bound clears $\beta = 1$ or a physical reserve gives $F_{\perp}(\xi) \geq F_0 > 0$ over the certified support, otherwise it must be accompanied by the regulator flow of Sec. IV. The protocol also records where the safe geometry lies: the first latent Fisher-zero boundary is $T_{\text{safe}} = \pi/(2\Lambda) = 1.57 \mu\text{s}$, the average-QFI time $T_{\text{avg}} = 2.11 \mu\text{s}$ sits *beyond* it inside the Fisher-glass region, and

the tail-certified optimizer selects $T_{\text{TC}} = 0.95 \mu\text{s}$ before it, with the safe phase, Fisher angle ψ , and transverse gain g_{\perp} of Secs. V–VI separating a certifiable schedule from a catastrophic one.

Physical repair and attainability (vi). The safe-window, portfolio, and reserve schedules are exactly the repairs of Sec. VII instantiated on hardware; the remaining repairs and the extrinsic regulators of Secs. IV and VII attach at the same point. Estimator attainability is confirmed by repeating the sensing block R times at fixed calibrated curvature and forming

$$\mathcal{A}_{\text{D}}(i) = n \widehat{\text{Var}}_r(\widehat{\theta}_{ir}) \widehat{F}_{i,\theta|\mu}, \quad (30)$$

where $r = 1, \dots, R$ indexes repeated sensing blocks at fixed ξ_i , $\widehat{\theta}_{ir}$ is the MLE in repeat r , $\widehat{\text{Var}}_r$ is the sample variance over those repeats, and n is the sensing-shot budget. This ratio concentrates near unity in the certified region while the average-QFI design is exposed by its inverse-loss tail. Sensitivity sweeps, finite-session convergence, Hill-exponent intervals, and a direct Fisher-loss versus MLE-error comparison are reported in the Supplemental Methods (Appendix Q, Figs. 5 and 6).

IX. DISCUSSION AND SCOPE

We have shown that latent non-self-averaging sensors require certification of the session-resolved attainable loss, not only the averaged Fisher response. The obstruction is not low average sensitivity but rare latent configurations in which usable information vanishes or becomes tangent to nuisance motion, and in general it cannot be inferred from averaged Fisher geometry (Theorem 1), and is moreover not even a renormalized Fisher matrix (Sec. III A). The certificate is governed by a sharp integrability transition at $\beta = 1$ (Theorem 2), the certified quantum resource is transverse to latent disorder (Theorem 3), and the repairs are geometric: zero-free windows, codimension raised by nondegenerate portfolios, configuration-wise reserves, signal-disorder action separation, and the weakest target-identifying Fisher cut (Theorem 4). The shallow-NV tournament shows that this certificate is experimentally estimable with finite calibration and sensing shots, and that it reverses the protocol ranking selected by average QFI.

Outside these assumptions the same six-step certification protocol of Sec. VIII remains diagnostic, with the explicit exponents and zero boundaries then model-dependent rather than universal. The boundary of the theory is also its reassurance: in self-averaging environments average Fisher information may remain the right design objective, whereas in latent non-self-averaging environments quantum enhancement must pass the stricter test of the quenched pipeline of Eq. (1). The certificate of quantum metrological advantage is then a property of the quenched Fisher geometry, not of any averaged channel.

X. AUTHOR CONTRIBUTIONS

E.M.M. conceived the project, developed the theoretical model, performed the numerical simulations, and wrote the manuscript. K.A. reviewed the manuscript, provided logistical support, and supervised the project. All authors contributed to the interpretation of the results and the finalization of the manuscript.

ACKNOWLEDGMENTS

This research was supported by JSPS KAKENHI Grant Number 24K21730.

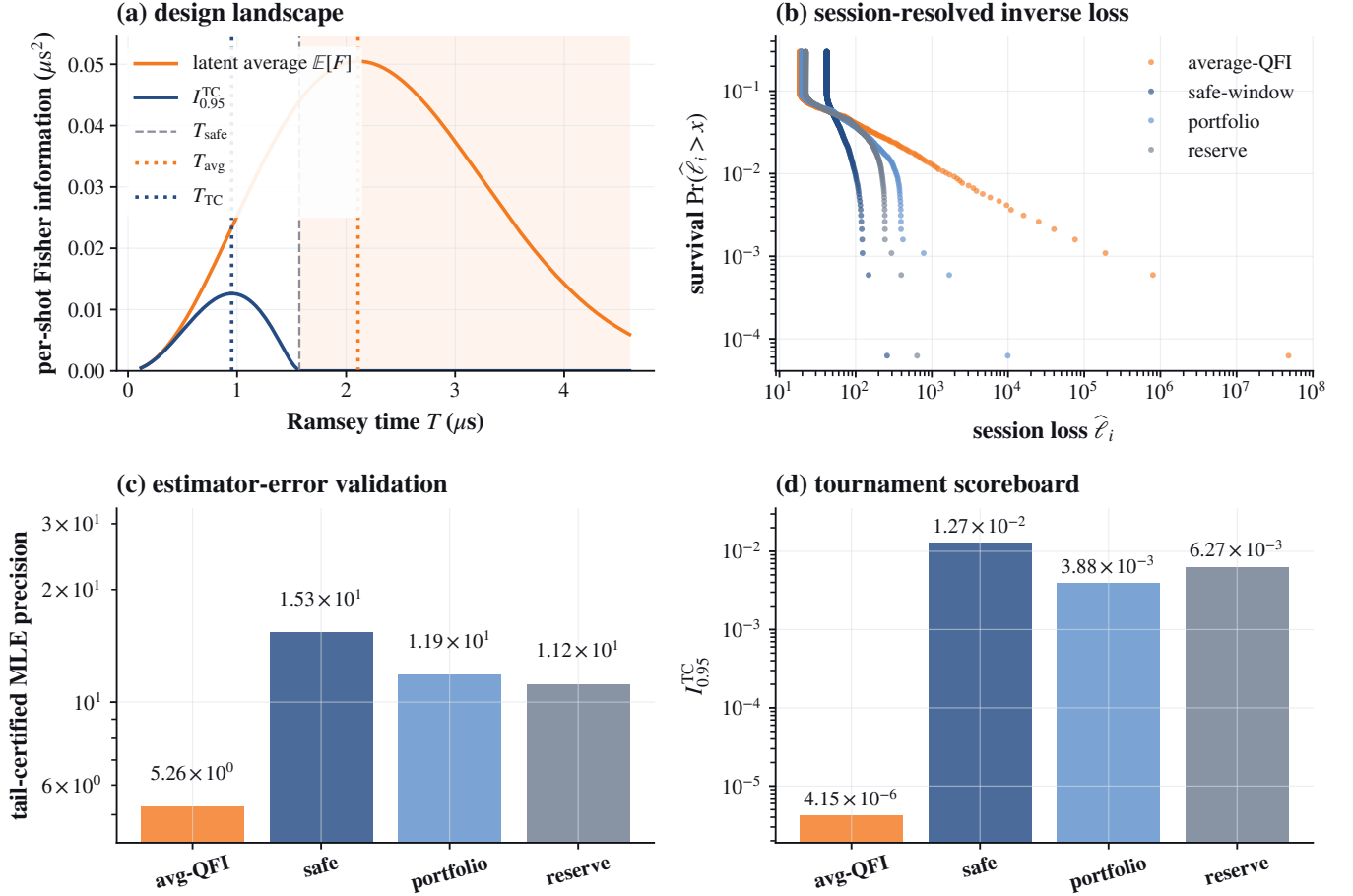


FIG. 4. **Annealed winner, quenched loser.** A platform-level shallow-NV design tournament compares four Ramsey protocols under the same shot budget and latent session ensemble. (a) The standard average-QFI rule selects $T_{\text{avg}} > T_{\text{safe}}$, crossing into the Fisher-glass region, while the tail-certified optimizer stays at $T_{\text{TC}} < T_{\text{safe}}$. (b) Session-resolved inverse-loss tails expose the mechanism: the average-QFI arm has a much heavier bad-session tail, while portfolio and reserve designs suppress the far tail. (c) With finite calibration shots, finite sensing shots, and an explicit MLE, the plotted tail-certified MLE precision $1/\text{CVaR}_{0.95}(\text{MSE}_{\text{MLE}})$ tracks the predicted ranking. (d) Scoreboard: safe-window, portfolio, and reserve designs recover nearly three orders of magnitude in $I_{0.95}^{\text{TC}}$ relative to the average-QFI design. This protocol-ranking reversal is the operational signature of the Fisher-glass regime.

TABLE II. Scope of the main statements.

Statement	Main assumptions	Status
CVaR-QCRB and tail-certified loss	Session-fixed latent configuration; local regularity; pointwise QCRB or Holevo bound	General certification bound
Nuisance-projected scalar resource	Regular nuisance block or Moore–Penrose support convention	Exact local scalar/directional statement
Geometric Fisher-zero exponent	Smooth latent density; codimension- c zero; local behavior $F \asymp r^{2m}$	Geometric tail law
Loschmidt-zero boundary	Pure-dephasing conditional coherence with real zeros in latent support	Model-specific mechanism for Fisher zeros
Portfolio exponent	Positive-channel decomposition; zero-nondegenerate active arms	Sparse/quasi-static tail law
Fisher reserve	Positive safe reference channel over the certified latent support	Configuration-wise sufficient repair
Action-separation scaling	Fixed safe latent phase; smooth contrast factors without adverse scaling	Scaling criterion
Shallow-NV simulation	Sparse slow RTN surface fluctuators and calibrated Ramsey contrast	Representative platform demonstration

SUPPLEMENTAL METHODS OVERVIEW

The Supplemental Methods provide the proof details, model-specific derivations, finite-regularization laws, additional platform robustness figures, and simulation algorithm supporting the main-text statements. Appendix A places the framework among neighboring metrological risk notions; Appendices B–C prove the certification bound and the no-averaged-Fisher theorem; Appendix D develops the Holevo target-map extension; Appendices E–I prove the architecture, codimension, Loschmidt-zero, and action-separation laws; Appendices J–P give the platform-specific derivations; and Appendices Q–R document the simulation and the regulator flow.

Appendix A: Comparison with neighboring metrological frameworks

The distinction from neighboring frameworks is the order forced by frozen latent sessions: condition on the session, project nuisance directions, form the attainable inverse loss, and only then certify its latent-session tail. Table III summarizes the comparison.

Appendix B: CVaR preliminaries and proof of the CVaR quantum Cramér–Rao bound

For a conditional local model with QFI matrix $J(\xi)$, the directional inverse-Fisher loss for a target direction w is

$$\ell_w(\xi) = \begin{cases} w^\top J(\xi)^+ w, & w \in \text{range } J(\xi), \\ +\infty, & w \notin \text{range } J(\xi). \end{cases} \quad (\text{B1})$$

Equivalently, the corresponding directional Fisher information is

$$F_w(\xi) = \ell_w(\xi)^{-1} = \min_{\phi: w^\top \phi = 1} \phi^\top J(\xi) \phi, \quad (\text{B2})$$

with $F_w = 0$ when the direction is locally unidentifiable. This is the formal convention behind the scalar and directional tail-certified information used in the main text.

CVaR has the dual representation

$$\begin{aligned} \text{CVaR}_\alpha(X) &= \sup_{h \in \mathcal{Q}_\alpha} \mathbb{E}[hX], \\ \mathcal{Q}_\alpha &= \{h : 0 \leq h \leq (1 - \alpha)^{-1}, \mathbb{E}h = 1\}. \end{aligned} \quad (\text{B3})$$

Monotonicity follows immediately. The pointwise quantum Cramér–Rao bound gives $R(\xi; \theta) \geq 1/[nF_Q(\theta, \xi)]$ for every latent configuration where local unbiasedness and regularity hold. Applying CVaR monotonicity gives Eq. (4). The multiparameter result follows from the pointwise bound $w^\top V(\xi; \theta)w \geq n^{-1}\ell_w(\xi)$, with the extended convention of (B1). If w is outside the range of

$J(\xi)$, the target direction is locally unidentifiable for that configuration and the right-hand side is $+\infty$.

For the non-matrical tail-certified body statement, duality gives

$$\text{CVaR}_\alpha(w^\top J(\xi)^{-1}w) = \sup_{h \in \mathcal{Q}_\alpha} w^\top \mathbb{E}[h(\xi)J(\xi)^{-1}]w. \quad (\text{B4})$$

This is the supremum of positive quadratic forms, hence convex and homogeneous of degree two. Its unit sub-level set is symmetric and convex. It is not generally quadratic: for two equally likely configurations with $J_1^{-1} = \text{diag}(1, 100)$ and $J_2^{-1} = \text{diag}(100, 1)$ at $\alpha = 1/2$, the risk function is $R(w) = \max\{w^\top J_1^{-1}w, w^\top J_2^{-1}w\}$. It violates the parallelogram identity and therefore cannot arise from a single matrix.

Appendix C: Noncommutation of latent certification

The distinction from ordinary nuisance projection and ordinary risk optimization can be stated as a noncommutation property. Let $J(\xi)$ be a latent session-resolved Fisher matrix and define the projected scalar information

$$F_{\theta|\mu}(\xi) = J_{\theta\theta}(\xi) - J_{\theta\mu}(\xi)J_{\mu\mu}(\xi)^{-1}J_{\mu\theta}(\xi). \quad (\text{C1})$$

Then the tail-certified information

$$\mathcal{I}_{\alpha, \theta|\mu}^{\text{TC}} = [\text{CVaR}_\alpha(F_{\theta|\mu}(\xi)^{-1})]^{-1} \quad (\text{C2})$$

is not determined by the averaged Fisher matrix $\bar{J} = \mathbb{E}_\xi[J(\xi)]$. In particular, there exist latent ensembles with the same \bar{J} and the same average projected information $\mathbb{E}_\xi[F_{\theta|\mu}(\xi)]$ but different tail-certified information, including one with $\mathcal{I}_{\alpha, \theta|\mu}^{\text{TC}} = 0$ and one with $\mathcal{I}_{\alpha, \theta|\mu}^{\text{TC}} > 0$.

It is enough to consider the scalar case and then embed the construction as the θ block of a larger Fisher matrix. One ensemble has $F(\xi) = 1$ deterministically, so its tail-certified information is finite. A second ensemble can be chosen with bounded support, with density nonzero near $F = 0$ so that F^{-1} has a nonintegrable upper tail, and with compensating mass at larger finite F so that $\mathbb{E}F = 1$ remains finite. The averaged Fisher matrix and average projected information are the same, but the CVaR of F^{-1} is infinite in the second ensemble. Thus latent certification depends on the projected inverse-loss tail, not on the averaged geometry.

Concretely, take ensemble A with $F_A = 1$ deterministically, so $\mathbb{E}F_A = 1$ and $\mathbb{E}[1/F_A] = 1$ (finite certificate). For ensemble B, let F_B be, with probability $\frac{1}{2}$, a draw from the density $p(F) = \frac{1}{2}F^{-1/2}$ on $(0, 1]$, and with probability $\frac{1}{2}$ a point mass at $F_0 = 5/3$. Then

$$\mathbb{E}F_B = \frac{1}{2} \int_0^1 F p(F) dF + \frac{1}{2}F_0 = \frac{1}{2} \cdot \frac{1}{3} + \frac{1}{2} \cdot \frac{5}{3} = 1, \quad (\text{C3})$$

matching ensemble A, whereas

$$\mathbb{E}[1/F_B] \geq \frac{1}{2} \int_0^1 F^{-1} p(F) dF = \frac{1}{4} \int_0^1 F^{-3/2} dF = \infty. \quad (\text{C4})$$

TABLE III. Comparison with neighboring metrological risk notions.

Framework	Random object	Risk/loss	Fisher-glass distinction
Average-QFI or decoherence-limited metrology	Self-averaged or fixed noisy channel	Average QFI / classical Fisher information (FI)	Can miss rare sessions where projected Fisher information nearly vanishes.
Nuisance-parameter metrology	Fixed local model with nuisance coordinates	Schur-complement or Holevo nuisance loss	Adds a quenched distribution of such losses across sessions.
Bayesian metrology	Prior over target and/or nuisance variables	Prior-averaged loss	Here θ is fixed locally; the risk is over frozen session labels.
Minimax robust metrology	Worst-case model element	Supremum loss	CVaR weights bad latent sessions by probability rather than only by worst case.
Compound/random-channel metrology	Family or mixture of channels	Channel-family or averaged-channel criterion	The loss is formed after conditioning on the frozen session, not on the annealed channel.
Finite-sample or outage-style metrology	Estimator outcome at finite sample size	Success probability, outage probability, or finite-sample accuracy	Tests finite-shot attainability of a target error; Fisher-glass risk is over session-to-session latent geometry and is applied to the conditional loss before estimator-error validation.
Fisher-glass certification	Frozen latent configuration ξ	$[\text{CVaR}_\alpha(\ell_{\mathcal{P}}(\xi))]^{-1}$	Condition, project nuisance, invert, then tail-certify.

Hence $\text{CVaR}_\alpha(1/F_B) = \infty$ and the certificate is zero, while ensembles A and B share $\mathbb{E}F = 1$ (the same averaged Fisher matrix and averaged projected information) yet differ in tail-certified information, one finite and one zero.

Appendix D: Holevo tail-certified extension

The symmetric logarithmic derivative (SLD) Fisher matrix need not give an attainable multiparameter bound when different target components require incompatible measurements. The attainable local asymptotic replacement is the Holevo loss after nuisance projection.

Let

$$\omega = (\theta, \mu), \quad \theta \in \mathbb{R}^p, \quad \mu \in \mathbb{R}^q, \quad (\text{D1})$$

and let ρ_ω^ξ be the conditional local model selected by the latent configuration ξ . The reported target need not be the full vector θ . We write

$$\vartheta = B\theta, \quad B \in \mathbb{R}^{d_B \times p}, \quad (\text{D2})$$

where B has full row rank, and use a positive definite weight $W_B \succ 0$ on the reported target. Full-vector estimation corresponds to $B = I_p$; directional estimation corresponds to $d_B = 1$ and $B = w^\top$. Equivalently, a rank-deficient weight $W \succeq 0$ on the original θ -space is represented by choosing B and W_B such that $W = B^\top W_B B$. The estimator is then required to be locally unbiased only for the reported target $B\theta$.

For fixed ξ , write $\rho = \rho_{\omega_0}^\xi$ and $\dot{\rho}_\eta = \partial_\eta \rho_\omega^\xi|_{\omega_0}$. Define

the admissible observable class

$$\begin{aligned} \mathcal{X}_{B|\mu}(\xi) = \{ & X = (X_a)_{a=1}^{d_B} : X_a = X_a^\dagger, \\ & \text{Tr}(\rho X_a) = 0, \\ & \text{Tr}(\dot{\rho}_{\theta_j} X_a) = B_{aj}, \\ & \text{Tr}(\dot{\rho}_{\mu_\ell} X_a) = 0 \}. \end{aligned} \quad (\text{D3})$$

For $X \in \mathcal{X}_{B|\mu}(\xi)$, set

$$Z_{ab}(X; \xi) = \text{Tr}(\rho X_a X_b). \quad (\text{D4})$$

The nuisance-projected Holevo loss for the reported target is

$$\begin{aligned} C_{B\theta|\mu}^H(W_B; \xi) = \inf_{X \in \mathcal{X}_{B|\mu}(\xi)} \left\{ & \text{tr}[W_B \text{Re } Z_X] \right. \\ & \left. + \left\| W_B^{1/2} \text{Im } Z_X W_B^{1/2} \right\|_1 \right\}. \end{aligned} \quad (\text{D5})$$

Here Z_X abbreviates $Z(X; \xi)$ inside the infimum. If $\mathcal{X}_{B|\mu}(\xi) = \emptyset$, or if a W_B -visible reported target direction is locally indistinguishable from nuisance motion, we set

$$C_{B\theta|\mu}^H(W_B; \xi) = +\infty. \quad (\text{D6})$$

The constraint $\text{Tr}(\dot{\rho}_{\mu_\ell} X_a) = 0$ is the nuisance-projection condition: the reported estimator is locally insensitive to nuisance displacements, while the nuisance remains part of the local statistical experiment.

Under the usual regularity assumptions for the Holevo bound, and when the completed local model is nonsingular, Eq. (D5) agrees with the corresponding zero-weight construction. In particular, for $B = I_p$ and $W \succ 0$,

$$C_{\theta|\mu}^H(W; \xi) = \lim_{\varepsilon \downarrow 0} C_{\theta, \mu}^H \left(\begin{pmatrix} W & 0 \\ 0 & \varepsilon I_q \end{pmatrix}; \xi \right). \quad (\text{D7})$$

Here $C_{\theta,\mu}^H$ denotes the ordinary Holevo loss for the completed target (θ, μ) . For a general target map B , one may complete B to a locally invertible change of target coordinates and assign vanishing weight to the unreported coordinates and to μ . The constrained definition (D5) is the primary definition and remains meaningful when unreported target directions are not locally identifiable.

For any locally asymptotically covariant estimator sequence of the reported target, with conditional covariance $V_{B,n}(\xi)$, assume the Holevo remainder is uniform over the safe latent support, or more generally that its negative part is $o(n^{-1})$ in CVaR. Then

$$\begin{aligned} & \liminf_{n \rightarrow \infty} n \text{CVaR}_\alpha(\text{Tr } W_B V_{B,n}(\xi)) \\ & \geq \text{CVaR}_\alpha\left(C_{B\theta|\mu}^H(W_B; \xi)\right). \end{aligned} \quad (\text{D8})$$

If the conditional model is quantum local asymptotic normality (QLAN)-regular and the Holevo bound is uniformly attainable over the safe latent support, with a CVaR-controlled remainder, then

$$\begin{aligned} & \lim_{n \rightarrow \infty} n \text{CVaR}_\alpha(\text{Tr } W_B V_{B,n}(\xi)) \\ & = \text{CVaR}_\alpha\left(C_{B\theta|\mu}^H(W_B; \xi)\right). \end{aligned} \quad (\text{D9})$$

Under these conditions the bound is tight at the level of the leading n^{-1} loss [41]. The vector-target tail-certified Holevo information is therefore

$$\mathcal{I}_{\alpha,B|\mu}^{\text{TC,H}}(W_B) = \left[\text{CVaR}_\alpha\left(C_{B\theta|\mu}^H(W_B; \xi)\right) \right]^{-1}. \quad (\text{D10})$$

Thus the vector-target Fisher-glass criterion is the tail integrability of the conditional attainable loss $C_{B\theta|\mu}^H(W_B; \xi)$, not the average SLD QFI matrix.

Let the SLD Fisher matrix of the full local model be block-decomposed as

$$J(\xi) = \begin{pmatrix} J_{\theta\theta} & J_{\theta\mu} \\ J_{\mu\theta} & J_{\mu\mu} \end{pmatrix}. \quad (\text{D11})$$

The nuisance-projected SLD Fisher matrix is

$$J_{\theta|\mu} = J_{\theta\theta} - J_{\theta\mu} J_{\mu\mu}^+ J_{\mu\theta}, \quad (\text{D12})$$

with the usual Moore–Penrose support convention on singular strata. The compatible SLD loss for the reported target is

$$C_{B\theta|\mu}^S(W_B; \xi) = \begin{cases} \text{tr} \left[W_B B J_{\theta|\mu}^+ B^\top \right], & \text{row}(B) \subseteq \\ & \text{range}(J_{\theta|\mu}), \\ +\infty, & \text{otherwise.} \end{cases} \quad (\text{D13})$$

The Holevo loss satisfies

$$C_{B\theta|\mu}^H(W_B; \xi) \geq C_{B\theta|\mu}^S(W_B; \xi). \quad (\text{D14})$$

If the nuisance-projected reported-target model is SLD-compatible, the inequality is saturated:

$$C_{B\theta|\mu}^H(W_B; \xi) = \text{tr} \left[W_B B J_{\theta|\mu}^+ B^\top \right]. \quad (\text{D15})$$

For a scalar reported target, $d_B = 1$, $B = w^\top$, $W_B = 1$, this gives

$$C_{w^\top\theta|\mu}^H(1; \xi) = w^\top J_{\theta|\mu}^+ w, \quad (\text{D16})$$

and for the original one-dimensional scalar case,

$$C_{\theta|\mu}^H(1; \xi) = F_{\theta|\mu}^{-1}(\xi). \quad (\text{D17})$$

When the compatible loss is finite and nonzero, define

$$\kappa_H(B, W_B; \xi) = \frac{C_{B\theta|\mu}^H(W_B; \xi)}{\text{tr} \left[W_B B J_{\theta|\mu}^+ B^\top \right]} \geq 1. \quad (\text{D18})$$

This separates projected identifiability loss from genuine measurement incompatibility. If near a Holevo-null set

$$C_{B\theta|\mu}^H(W_B; s, u) \asymp r^{-\sigma} \quad (\text{D19})$$

in codimension c (with $\sigma = 2m$ for a Fisher zero of order m , matching the $2m$ of Eq. (11)), and the latent density scales as r^ν , then

$$\Pr\left(C_{B\theta|\mu}^H(W_B; \xi) > x\right) \asymp x^{-(c+\nu)/\sigma}. \quad (\text{D20})$$

Therefore finite vector-target tail certification requires

$$\frac{c+\nu}{\sigma} > 1. \quad (\text{D21})$$

For a simple codimension-one Fisher zero with bounded κ_H , $\sigma = 2$, hence the inverse-loss survival exponent is $1/2$, and all finite-level CVaR losses diverge.

As a minimal vector example, consider the local pure-qubit model

$$|\psi_{\theta,\xi}\rangle = |0\rangle + \frac{a(\xi)}{2}(\theta_1 + i\theta_2)|1\rangle + O(|\theta|^2). \quad (\text{D22})$$

At $\theta = 0$, $J_{\theta\theta} = a(\xi)^2 I_2$. For the full two-component target, $B = I_2$, $W_B = I_2$, the compatible SLD loss is $2/a(\xi)^2$. The two-parameter pure-qubit Holevo–Nagaoka bound gives

$$C_{\theta}^H(I_2; \xi) = \frac{4}{a(\xi)^2}, \quad (\text{D23})$$

so $\kappa_H = 2$. For a one-dimensional reported direction $B = w^\top$, the problem is scalar and

$$C_{w^\top\theta}^H(1; \xi) = \frac{|w|^2}{a(\xi)^2}. \quad (\text{D24})$$

If an unknown nuisance coordinate shifts only the first quadrature,

$$|\psi_{\theta,\mu,\xi}\rangle = |0\rangle + \frac{a(\xi)}{2}((\theta_1 + \mu) + i\theta_2)|1\rangle + O(|\theta|^2 + |\mu|^2), \quad (\text{D25})$$

then $\dot{\rho}_{\theta_1}^\xi = \dot{\rho}_\mu^\xi$. The full target (θ_1, θ_2) is not identifiable after nuisance projection, so $C_{\theta|\mu}^H(I_2; \xi) = +\infty$. However

the reported target $B = e_2^\top$ remains identifiable, with admissible observable $X = \sigma_y/a(\xi)$ and

$$C_{e_2^\top \theta | \mu}^H(1; \xi) = \frac{1}{a(\xi)^2}. \quad (\text{D26})$$

Thus the target-map formulation distinguishes an unidentifiable full target from an identifiable reported target.

Quantum nuisance-parameter treatments and practical evaluations of the Holevo bound provide the corresponding tools for vector targets [21, 40].

Appendix E: Proof of the Fisher-cut theorem

For a cut S , there exists ϕ_S with $a_e^\top \phi_S = 0$ for $e \notin S$ and $w^\top \phi_S \neq 0$. Normalize $w^\top \phi_S = 1$. Then $F_w \leq \sum_{e \in S} g_e (a_e^\top \phi_S)^2 \leq C_S \sum_{e \in S} g_e$, and minimizing over cuts gives the upper bound.

For the lower bound, consider every subset $T \subseteq E$ spanning w and choose coefficients $c_e^{(T)}$ with $w = \sum_{e \in T} c_e^{(T)} a_e$. Since there are finitely many spanning subsets, choose $\delta > 0$ so that $\sum_{e \in T} |c_e^{(T)}| \delta < 1$ for all of them. For any feasible ϕ , let $S_\phi = \{e : |a_e^\top \phi| \geq \delta\}$. If $E \setminus S_\phi$ spanned w , then $|w^\top \phi| < 1$, contradiction. Thus S_ϕ is a cut, and $\sum_e g_e (a_e^\top \phi)^2 \geq \delta^2 \Phi_w$. Minimizing over ϕ gives the lower bound.

For a fixed cut S , independence and $\mathbb{P}(g_e < \varepsilon) = \varepsilon^{\eta_e + o(1)}$ imply $\mathbb{P}(\sum_{e \in S} g_e < \varepsilon) = \varepsilon^{\sum_{e \in S} \eta_e + o(1)}$. A finite union over cuts is dominated by the smallest exponent. Setting $\varepsilon = x^{-1}$ proves the tail law.

Appendix F: Nuisance-projected Fisher cuts and transverse Fisher volume

This appendix records the multiparameter geometry behind the signal-disorder action-separation law. It should be read as a regular-stratum statement: the nuisance block is assumed nonsingular on the configurations under consideration, while the extended inverse-Fisher convention applies when the target direction is not identifiable.

Proposition 2 (Nuisance-projected Fisher cuts). *Consider one target coordinate θ and q nuisance coordinates μ . Let*

$$J(\xi) = \sum_{e \in E} g_e(\xi) b_e b_e^\top, \quad g_e(\xi) \geq 0, \quad (\text{F1})$$

$$b_e = (s_e, n_e^\top) \in \mathbb{R}^{q+1}.$$

Assume the nuisance block is nonsingular on the relevant support. The nuisance-projected Fisher information for θ is

$$F_{\theta | \mu}(\xi) = J_{\theta\theta} - J_{\theta\mu} J_{\mu\mu}^{-1} J_{\mu\theta}. \quad (\text{F2})$$

Let B_S denote the $(q+1) \times (q+1)$ matrix with rows b_e^\top , $e \in S$, and let N_R denote the $q \times q$ matrix with rows n_e^\top , $e \in R$. Then

$$F_{\theta | \mu} = \frac{\sum_{|S|=q+1} (\prod_{e \in S} g_e) \det(B_S)^2}{\sum_{|R|=q} (\prod_{e \in R} g_e) \det(N_R)^2}, \quad (\text{F3})$$

with the empty determinant convention for $q = 0$.

A nuisance-projected Fisher cut is a subset $C \subset E$ such that, after removing C , the target response of every remaining channel can be absorbed into the nuisance span:

$$C \in \mathcal{C}_{\theta | \mu} \iff \exists u_C \in \mathbb{R}^q \text{ such that} \quad (\text{F4})$$

$$s_e + n_e^\top u_C = 0 \quad \text{for all } e \notin C.$$

Equivalently, the restricted signal vector lies in the range of the restricted nuisance-response matrix. Define

$$\Phi_{\theta | \mu}(\xi) = \min_{C \in \mathcal{C}_{\theta | \mu}} \sum_{e \in C} g_e(\xi). \quad (\text{F5})$$

For fixed finite response vectors, on the same regular stratum, if the target is identifiable before any channel failure, there are constants $0 < c_{\theta | \mu} < C_{\theta | \mu} < \infty$ such that

$$c_{\theta | \mu} \Phi_{\theta | \mu}(\xi) \leq F_{\theta | \mu}(\xi) \leq C_{\theta | \mu} \Phi_{\theta | \mu}(\xi). \quad (\text{F6})$$

If the channel weights are independent and

$$\mathbb{P}(g_e < \varepsilon) = \varepsilon^{\eta_e + o(1)}, \quad \varepsilon \rightarrow 0, \quad (\text{F7})$$

then

$$\mathbb{P}(F_{\theta | \mu}^{-1} > x) = x^{-\beta_{\theta | \mu} + o(1)}, \quad \beta_{\theta | \mu} = \min_{C \in \mathcal{C}_{\theta | \mu}} \sum_{e \in C} \eta_e. \quad (\text{F8})$$

Thus finite nuisance-projected tail-certified information requires $\beta_{\theta | \mu} > 1$.

Proof. The Schur complement identity $F_{\theta | \mu} = \det J / \det J_{\mu\mu}$, together with Cauchy–Binet applied to $J = D^\top G D$ and $J_{\mu\mu} = N^\top G N$, gives (F3). Equivalently,

$$F_{\theta | \mu} = \min_{u \in \mathbb{R}^q} \sum_{e \in E} g_e (s_e + n_e^\top u)^2. \quad (\text{F9})$$

For the upper bound, take a nuisance-projected Fisher cut C . By definition, there exists u_C such that $s_e + n_e^\top u_C = 0$ for $e \notin C$. Hence

$$F_{\theta | \mu} \leq \sum_{e \in C} g_e (s_e + n_e^\top u_C)^2 \leq C_C \sum_{e \in C} g_e. \quad (\text{F10})$$

Minimizing over C gives the upper bound in (F6).

For the lower bound, finiteness of E and fixed response vectors imply that there is a $\delta > 0$ such that whenever a subset $T \subset E$ is not target-absorbable,

$$\inf_u \max_{e \in T} |s_e + n_e^\top u| \geq \delta. \quad (\text{F11})$$

For any u , let $S(u) = \{e : |s_e + n_e^\top u| \geq \delta\}$. Then $E \setminus S(u)$ cannot be nonabsorbable, since all its residuals are smaller than δ . Therefore $S(u) \in \mathcal{C}_{\theta|\mu}$. Thus

$$\sum_e g_e (s_e + n_e^\top u)^2 \geq \delta^2 \sum_{e \in S(u)} g_e \geq \delta^2 \Phi_{\theta|\mu}. \quad (\text{F12})$$

Minimizing over u gives the lower bound.

For a fixed cut C , independence and (F7) give $\mathbb{P}(\sum_{e \in C} g_e < \varepsilon) = \varepsilon^{\sum_{e \in C} \eta_e + o(1)}$. A finite union over nuisance-projected cuts is dominated by the smallest exponent, and (F6) transfers the exponent to $F_{\theta|\mu}$. Setting $\varepsilon = x^{-1}$ proves (F8).

Corollary 1 (Critical transverse scaling). *Consider a family of sensors indexed by size L . Suppose that on a regular nuisance stratum the projected signal gain and disorder action gain obey*

$$g_\perp(L) \sim L^{y_\perp}, \quad g_d(L) \sim L^{y_d}. \quad (\text{F13})$$

Assume that the safe latent phase optimum remains L -independent, that the smooth contrast factor has no adverse scaling, and that no additional Fisher-zero singularity is introduced by the transverse angle. Then the optimized per-shot tail-certified information scales as

$$\mathcal{I}_{\alpha, \text{shot}}^{\text{TC}}(L) \sim L^{2(y_\perp - y_d)}. \quad (\text{F14})$$

If $g_s(L) \sim L^{y_s}$ and $\sin^2 \psi_L \sim L^{-\delta}$, then $y_\perp = y_s - \delta/2$, so

$$\mathcal{I}_{\alpha, \text{shot}}^{\text{TC}}(L) \sim L^{2(y_s - y_d) - \delta}. \quad (\text{F15})$$

With negligible dead time, the information rate scales as

$$\Gamma_\alpha^{\text{TC}}(L) \sim L^{2y_\perp - y_d}. \quad (\text{F16})$$

Proof. At fixed safe latent phase $\Phi = g_d(L)T\Lambda$, the interrogation time scales as $T = \Phi/[g_d(L)\Lambda]$. The projected Fisher scale is $g_\perp^2(L)T^2$ times an L -independent dimensionless tail factor. Therefore the inverse-CVaR scale is proportional to $(g_\perp/g_d)^2$. The rate statement follows by dividing by T in the negligible-dead-time limit.

Generic volume-hypergraph consequence. When the nuisance response rows are in generic position, so that every subset of at most q nuisance rows has full row rank and every larger subset has rank q , the target-absorption cuts are exactly the vertex covers of the nonzero $(q+1)$ -volume hypergraph. For K generic channels in \mathbb{R}^{q+1} , every $(q+1)$ -tuple has nonzero Fisher volume. Destroying all transverse volumes then requires leaving at most q channels, so the smallest cut has size $K-q$. For identical simple-zero channels, $\eta_e = 1/2$, and therefore

$$\beta_{\theta|\mu} = \frac{K-q}{2}. \quad (\text{F17})$$

Finite CVaR requires $\beta_{\theta|\mu} > 1$, hence

$$K \geq q + 3. \quad (\text{F18})$$

The case $q = 0$ recovers the scalar portfolio threshold $K \geq 3$; one nuisance direction raises the generic threshold to $K \geq 4$.

Appendix G: Proof of the Fisher-codimension law

The event $\ell > x$ is $F < x^{-1}$. Near Z , this is equivalent to $r \lesssim A(s, \hat{u})^{-1/(2m)} x^{-1/(2m)}$. The tube probability is asymptotic to

$$\int_Z \int_{S^{c-1}} \int_0^{A(s, \hat{u})^{-1/(2m)} x^{-1/(2m)}} b_0(s, \hat{u}) r^{c-1+\nu} dr d\hat{u} d\sigma(s), \quad (\text{G1})$$

which equals $A_\eta x^{-(c+\nu)/(2m)}$ with finite positive A_η . The moment criterion follows from $\mathbb{E}[\ell^s] = s \int_0^\infty x^{s-1} \mathbb{P}(\ell > x) dx$.

Appendix H: Proof of the Loschmidt-zero transition

Let $u = A\lambda$ and suppose $\chi(u) = a(u - u_1)^m + o(|u - u_1|^m)$ at the first positive real zero u_1 . If $A\lambda \geq u_1$, then $\lambda_* = u_1/A$ lies in the latent support. Near λ_* ,

$$\begin{aligned} F_A(\lambda) &= A^2 C_A^2 |\chi(A\lambda)|^2 \\ &= C_A^2 |a|^2 |A|^{2m+2} |\lambda - \lambda_*|^{2m} + o(|\lambda - \lambda_*|^{2m}). \end{aligned} \quad (\text{H1})$$

Therefore $1/F_A > x$ is equivalent, to leading order, to $|\lambda - \lambda_*| < c_0 x^{-1/(2m)}$ for a positive constant c_0 . If the coupling density is continuous and nonzero at λ_* , the probability of this interval is asymptotic to $2p(\lambda_*)c_0 x^{-1/(2m)}$ for an interior zero and half this value at a support endpoint. Since $1/(2m) \leq 1/2 < 1$, the first inverse-Fisher moment and every CVaR level $\alpha < 1$ diverge. If $A\lambda < u_1$, compactness of $[0, \Lambda]$ and continuity of χ imply $\min_{\lambda \in [0, \Lambda]} |\chi(A\lambda)| > 0$, so $1/F_A$ is bounded.

Appendix I: Proof of the signal-disorder action separation law

For $\Phi = g_d(M)T\Lambda$ and $U = \lambda/\Lambda$, the pure-dephasing Fisher information $F_M(T, \lambda) = g_s(M)^2 T^2 C_M^2(T) |\chi(g_d(M)T\lambda)|^2$ can be rewritten as

$$F_M(T, \lambda) = \left(\frac{g_s(M)}{g_d(M)} \right)^2 \frac{C_M^2(T)}{\Lambda^2} \Phi^2 |\chi(\Phi U)|^2. \quad (\text{I1})$$

The prefactor is deterministic with respect to the latent variable, so positive homogeneity of CVaR gives

$$\begin{aligned} \text{CVaR}_\alpha \left(\frac{1}{F_M} \right) &= \left(\frac{g_d(M)}{g_s(M)} \right)^2 \frac{\Lambda^2}{C_M^2(T)} \\ &\quad \times \text{CVaR}_\alpha \left(\frac{1}{\Phi^2 |\chi(\Phi U)|^2} \right). \end{aligned} \quad (\text{I2})$$

Taking the inverse gives the action-separation law stated in the main text. If $\Phi \geq u_1$, then $U_* = u_1/\Phi$ lies in $[0, 1]$. When the induced density is nonzero there, one-sidedly if $U_* = 1$, and the zero has finite order, the same

local calculation as in the Loschmidt-zero transition gives a nonintegrable inverse-Fisher tail, hence infinite CVaR and zero tail-certified information.

Appendix J: RTN coherence and exact safety threshold

For a symmetric RTN process $n(t) = \pm 1$ switching at rate γ_{RTN} , define $g_{\pm}(t) = \mathbb{E}[\exp(i\lambda \int_0^t n(s) ds) \mid n(0) = \pm 1]$. The sum $S = g_+ + g_-$ obeys

$$\dot{S} + 2\gamma_{\text{RTN}}\dot{S} + \lambda^2 S = 0, \quad S(0) = 2, \quad \dot{S}(0) = 0. \quad (\text{J1})$$

For $\lambda > \gamma_{\text{RTN}}$ this gives

$$\begin{aligned} W_{\text{RTN}}(T; \lambda, \gamma_{\text{RTN}}) &= e^{-\gamma_{\text{RTN}}T} \left[\cos(\Omega T) + \frac{\gamma_{\text{RTN}}}{\Omega} \sin(\Omega T) \right], \\ \Omega &= \sqrt{\lambda^2 - \gamma_{\text{RTN}}^2}. \end{aligned} \quad (\text{J2})$$

Zeros solve

$$\begin{aligned} \cos(\Omega T) + \frac{\gamma_{\text{RTN}}}{\Omega} \sin(\Omega T) &= 0, \\ \Omega &= \sqrt{\lambda^2 - \gamma_{\text{RTN}}^2}. \end{aligned} \quad (\text{J3})$$

The first zero is

$$T_{\text{zero}}(\lambda, \gamma_{\text{RTN}}) = \frac{\pi/2 + \arcsin(\gamma_{\text{RTN}}/\lambda)}{\sqrt{\lambda^2 - \gamma_{\text{RTN}}^2}}, \quad (\text{J4})$$

which decreases with λ . To see monotonicity, write $\delta = \gamma_{\text{RTN}}/\lambda$ and $T_{\text{zero}}(\lambda, \gamma_{\text{RTN}}) = h(\delta)/\lambda$, with $h(\delta) = (\pi/2 + \arcsin \delta)/\sqrt{1 - \delta^2}$. Since $h > 0$ and $h' > 0$ for $0 \leq \delta < 1$, $dT_{\text{zero}}/d\lambda = -(h + \delta h')/\lambda^2 < 0$. Therefore the strongest coupling Λ sets the first zero entering the support,

$$T_{\text{safe}}(\Lambda, \gamma_{\text{RTN}}) = \frac{\pi/2 + \arcsin(\gamma_{\text{RTN}}/\Lambda)}{\sqrt{\Lambda^2 - \gamma_{\text{RTN}}^2}}. \quad (\text{J5})$$

When $\gamma_{\text{RTN}} \geq \lambda$, the hyperbolic continuation is a positive sum of hyperbolic functions and has no real zero; hence the zero-driven divergence is absent in the motional-narrowing regime $\gamma_{\text{RTN}} \geq \Lambda$.

Appendix K: Ramsey QFI derivation

At the optimal working point, the Ramsey output state has Bloch vector length $\mathcal{W}(T, \xi)$ and signal phase speed T . The quantum Fisher information for the phase parameter is therefore $F_Q = T^2 \mathcal{W}^2(T, \xi)$. Measuring in the quadrature basis at the working point saturates this QFI to leading order, so the same conditional Fisher information appears in the classical readout.

Appendix L: Bernoulli sparse-bath approximation and reserve allocation

In the low-occupancy approximation $N = 0$ with probability $1 - N_f$ and $N = 1$ with probability N_f , the quasi-static scalar loss is $a = 1/[nT^2 C_0^2(T)]$ for $N = 0$ and $a \sec^2(\lambda T)$ for $N = 1$. For $\Lambda T < \pi/2$ and $\alpha < 1 - N_f$,

$$\text{CVaR}_{\alpha}(1/F_Q) = a \left[1 + \frac{N_f}{1 - \alpha} \left(\frac{\tan(\Lambda T)}{\Lambda T} - 1 \right) \right], \quad (\text{L1})$$

This gives the closed-form design expression used for the single-arm T_{TC} optimization. For a safe reserve anchor, the Poisson moment-generating function gives (N2); the first-moment bound gives the sufficient shot rule

$$n_0 \geq \frac{\exp[N_f(\sec^2(\Lambda T_0) - 1) + 2(T_0/T_2^*)^2]}{(1 - \alpha)RT_0^2}. \quad (\text{L2})$$

Here R is the target upper bound on the reserve contribution to the CVaR loss.

Appendix M: Proof of the Ramsey portfolio theorem

For K Ramsey arms with positive shot allocations, the quasi-static sparse Poisson portfolio Fisher information is

$$F_{\text{port}}(\xi) = \sum_{j=1}^K n_j T_j^2 C_0^2(T_j) \prod_{r=1}^N \cos^2(\lambda_r T_j). \quad (\text{M1})$$

For arm j , the zero grid inside the coupling support is

$$\mathcal{G}_j := \left\{ \frac{(2k+1)\pi}{2T_j} : k = 0, 1, 2, \dots \right\} \cap [0, \Lambda]. \quad (\text{M2})$$

Condition on N active fluctuators. The zero set of Eq. (M1) is a finite union of strata on which every arm is zeroed by at least one coupling coordinate. Zeronondegeneracy of the grids \mathcal{G}_j implies that a single coupling coordinate cannot zero two different arms. Therefore the generic portfolio-zero strata require K distinct coupling coordinates, one per arm, and have codimension K .

Near such a generic stratum choose normal coordinates $u_j = \lambda_{r_j} - \lambda_j^*$ with $\lambda_j^* \in \mathcal{G}_j$. Since $\cos(\lambda T_j) = \pm T_j u_j + O(u_j^2)$ at a simple zero,

$$F_{\text{port}}(\xi) = \sum_{j=1}^K b_j u_j^2 + O(\|u\|^3), \quad b_j > 0, \quad (\text{M3})$$

after fixing all tangential coordinates away from additional zeros. The volume of the set $\sum_j b_j u_j^2 < x^{-1}$ is proportional to $x^{-K/2}$. The coupling density is bounded above and below by positive constants at the chosen zeros, so the same exponent holds for the conditional probability. Strata involving repeated fluctuators, multiple

zeros associated with the same arm, or accidental additional constraints do not lower the logarithmic tail exponent below $K/2$. Under zero-nondegeneracy, the leading generic event is one independent simple zero per arm; nongeneric strata contribute only subleading constants or logarithmic corrections. Summing over the Poisson distribution of N changes the leading constant but not the logarithmic exponent. In the sparse limit the first nonzero generic contribution comes from $N \geq K$ and is proportional to N_f^K .

Appendix N: Proof of the Fisher reserve theorem

For the safe anchor, $T_0 < T_{\text{safe}}$ implies $m_0 = \min_{\lambda \in [0, \Lambda]} |W_{\text{RTN}}(T_0; \lambda, \gamma_{\text{RTN}})| > 0$. Therefore the anchor contribution obeys

$$F_0(\xi) = n_0 T_0^2 C_0^2(T_0) \prod_{k=1}^N W_{\text{RTN}}^2(T_0; \lambda_k, \gamma_{\text{RTN}}) \geq a_0 m_0^{2N}. \quad (\text{N1})$$

All other Fisher contributions are nonnegative, hence $F_{\text{tot}} \geq F_0$ and $\ell_{\text{tot}} \leq a_0^{-1} m_0^{-2N}$. Raising to power $s > 0$ and using the Poisson moment-generating function gives

$$\mathbb{E}[\ell_{\text{tot}}^s] \leq a_0^{-s} \mathbb{E}[m_0^{-2sN}] = a_0^{-s} \exp[N_f(m_0^{-2s} - 1)]. \quad (\text{N2})$$

The first moment is finite, hence every CVaR level below one is finite for the nonnegative loss. The super-polynomial tail follows by comparing ℓ_{tot} to $C\kappa^N$ and applying standard Poisson tail asymptotics.

Appendix O: Hahn echo proof

The Hahn-echo RTN coherence can be derived by propagating the RTN transfer matrix through two intervals of length $T/2$ with opposite signs of the coupling. In the oscillatory regime, let $\tau = T/2$, $c = \cos(\Omega\tau)$, $s = \sin(\Omega\tau)$, and $\epsilon = e^{-\gamma_{\text{RTN}}\tau}$. The transfer matrix for the first half is

$$A_{+\lambda}(\tau) = \epsilon \begin{pmatrix} c + i(\lambda/\Omega)s & (\gamma_{\text{RTN}}/\Omega)s \\ (\gamma_{\text{RTN}}/\Omega)s & c - i(\lambda/\Omega)s \end{pmatrix}, \quad (\text{O1})$$

and $A_{-\lambda}$ is obtained by replacing λ by $-\lambda$. With a uniform initial RTN state,

$$W_{\text{echo}}(T) = \frac{1}{2}(1, 1)A_{-\lambda}(\tau)A_{+\lambda}(\tau) \begin{pmatrix} 1 \\ 1 \end{pmatrix}, \quad (\text{O2})$$

which evaluates to

$$W_{\text{echo}}(T; \lambda, \gamma_{\text{RTN}}) = e^{-\gamma_{\text{RTN}}T} \left[\left(c + \frac{\gamma_{\text{RTN}}}{\Omega} s \right)^2 + \frac{\lambda^2}{\Omega^2} s^2 \right]. \quad (\text{O3})$$

Replacing $\Omega \rightarrow i\Omega_h$, and writing $c_h = \cosh(\Omega_h\tau)$ and $s_h = \sinh(\Omega_h\tau)$, gives

$$W_{\text{echo}}(T; \lambda, \gamma_{\text{RTN}}) = e^{-\gamma_{\text{RTN}}T} \left[\left(c_h + \frac{\gamma_{\text{RTN}}}{\Omega_h} s_h \right)^2 + \frac{\lambda^2}{\Omega_h^2} s_h^2 \right], \quad (\text{O4})$$

with $\Omega_h = \sqrt{\gamma_{\text{RTN}}^2 - \lambda^2}$. In the oscillatory formula, the bracket is a sum of two squares; if the sine term vanishes, then the cosine term is ± 1 , so the bracket is nonzero. In the hyperbolic formula the first square is strictly positive. Thus the single-fluctuator echo coherence has no real zero in the stated model.

Appendix P: Same-axis DC sensing bound

Let $y(t) = \pm 1$ be a pulse toggling function and $A_y = \int_0^T y(t) dt$. In the quasi-static scalar model, $W_y(\lambda) = \cos(\lambda A_y)$ and $F_Q^{(y)}(\lambda) = A_y^2 \cos^2(\lambda A_y)$. Avoiding coherence zeros for all $\lambda \in [0, \Lambda]$ requires $|A_y| < \pi/(2\Lambda)$, which implies $F_Q^{(y)}(\lambda) < \pi^2/(4\Lambda^2)$. If this condition is violated and the coupling density is nonzero at the first zero, the simple-zero $x^{-1/2}$ inverse-Fisher tail follows from the Fisher-codimension law.

Appendix Q: Finite-sample simulation details

Supplementary platform robustness figures. Figure 5 varies the main experimental knobs around Table I. The distinction is controlled most sharply by ΔT_2^* : below the zero-crossing threshold the average-QFI optimum remains inside the safe window and the ranking difference is modest, while above it the average-QFI tail certificate collapses and the safe-window certificate remains strongly favorable across the swept density, CVaR level, readout contrast, calibration-shot, and wall-clock settings.

Figure 6 checks finite-sample robustness. Increasing the number of latent sessions stabilizes the certified designs while the unsafe average-QFI arm continues to sample rarer near-zero sessions. Hill intervals place the unsafe arm below the $\beta = 1$ integrability boundary, and the direct MLE-error comparison shows that calibrated Fisher-loss CVaR tracks the actual estimator ranking once finite-estimator regularization is included.

Platform-level simulation algorithm. The shallow-NV platform demonstration uses the following measurement-level simulation. The input parameters are

$$N_{\text{sess}}, n, n_{\text{cal}}, T_2^*, c_{\text{ro}}, N_f, \Lambda, \theta_0, \\ \mathcal{T} = \{(T_k, w_k)\}.$$

The executable implementation is split into a slow experiment/cache script and a fast figure-rendering script. Running `python numerics/tail_certification_experiments.py --figure all` reruns the manuscript simulations, writes fixed numerical caches to `numerics/output/data/`, and writes processed summaries to `numerics/output/results.json` and `numerics/output/data/plot_cache_manifest.json`. Style-only figure changes can then be rendered

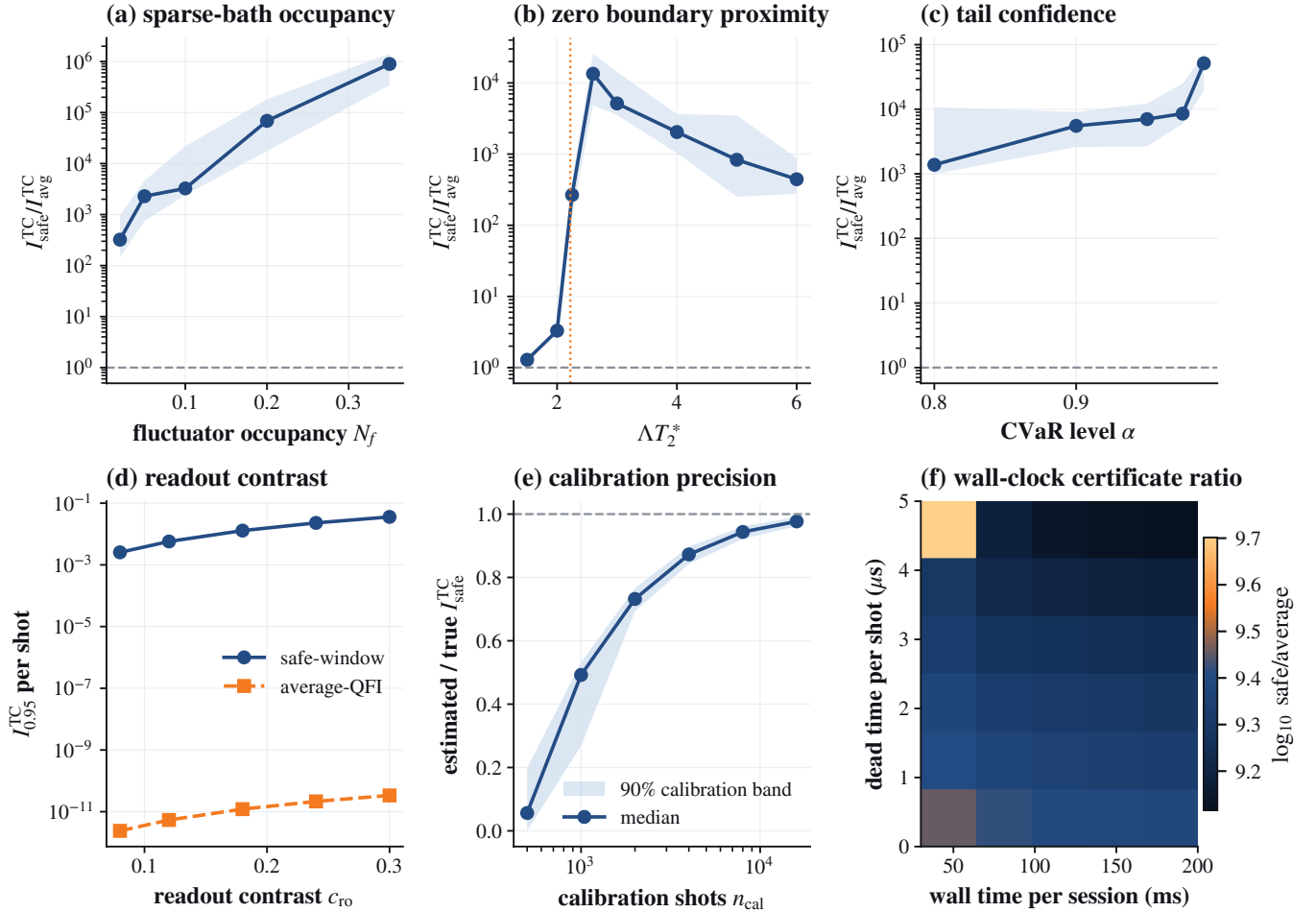


FIG. 5. **Sensitivity of the platform-level certificate.** Sweeps around the representative shallow-NV parameters in Table I. (a)–(c) The finite-session ratio of safe-window to average-QFI tail-certified information is shown as the median over 24 independent latent ensembles with $N_{\text{sess}} = 32000$ sessions each. Shading gives a 90% bootstrap confidence interval for the median log-ratio; the raw 10–90% ensemble spread is reported in the processed results file. The panels vary fluctuator occupancy N_f , dimensionless coupling range ΛT_2^* , and CVaR level α . The dotted line in (b) marks $\Lambda T_2^* = \pi/\sqrt{2}$, where the leading average-QFI optimum first crosses the quasi-static safety boundary. (d) Readout contrast scales the absolute certificates but does not remove the ranking reversal. (e) Finite calibration shots bias the empirical safe-window certificate low at small n_{cal} and converge toward the true session-resolved certificate as the calibration block grows. (f) With a fixed wall-clock budget per session, including calibration overhead and dead time per shot, the safe-window advantage persists over the swept time budgets.

without rerunning the experiments by `python numerics/tail_certification_figures.py --figure all`. All pseudorandom numbers use NumPy `default_rng` with base seed 20260430.

The one-arm times are selected by the same finite design tournament used in the plotted baseline. A separate *design* ensemble of $N_{\text{design}} = 2600$ latent configurations is drawn with the Fig. 4 stream, distinct from the $N_{\text{sess}} = 32000$ sessions used to evaluate the tournament. The grid $T \in [0.12, 4.6] \mu\text{s}$ has 260 equally spaced points. The average-QFI time T_{avg} maximizes $N_{\text{design}}^{-1} \sum_{i=1}^{N_{\text{design}}} (c_{\text{ro}} C_i(T) T)^2$ on this grid. The CVaR time T_{TC} maximizes $\widehat{T}_{0.95}^{\text{TC}}(T) = 1/\widehat{\text{CVaR}}_{0.95}\{[c_{\text{ro}} C_i(T) T]^{-2}\}$ over $T < T_{\text{safe}} = \pi/(2\Lambda)$,

with the certificate set to zero outside the safe window. This gives $T_{\text{avg}} = 2.109189 \mu\text{s}$ and $T_{\text{TC}} = 0.950270 \mu\text{s}$ for the Table I baseline.

The four fixed tournament protocols are: average-QFI, $(T, w) = (T_{\text{avg}}, 1)$; safe-window, $(T, w) = (T_{\text{TC}}, 1)$; portfolio, $T = (1.85, 2.20, 2.65) \mu\text{s}$ with equal weights; and reserve, $T = (1.00, T_{\text{avg}}) \mu\text{s}$ with weights (0.30, 0.70). For $n = 2000$ sensing shots the integer shot allocations are respectively 2000, 2000, (666, 666, 668), and (600, 1400); integer counts are formed by flooring nw_k and assigning the residual shots to the last arm. For each session $i = 1, \dots, N_{\text{sess}}$:

1. Draw $N_i \sim \text{Poisson}(N_f)$.
2. Draw latent couplings $\lambda_{ij} \sim \text{Uniform}[0, \Lambda]$.

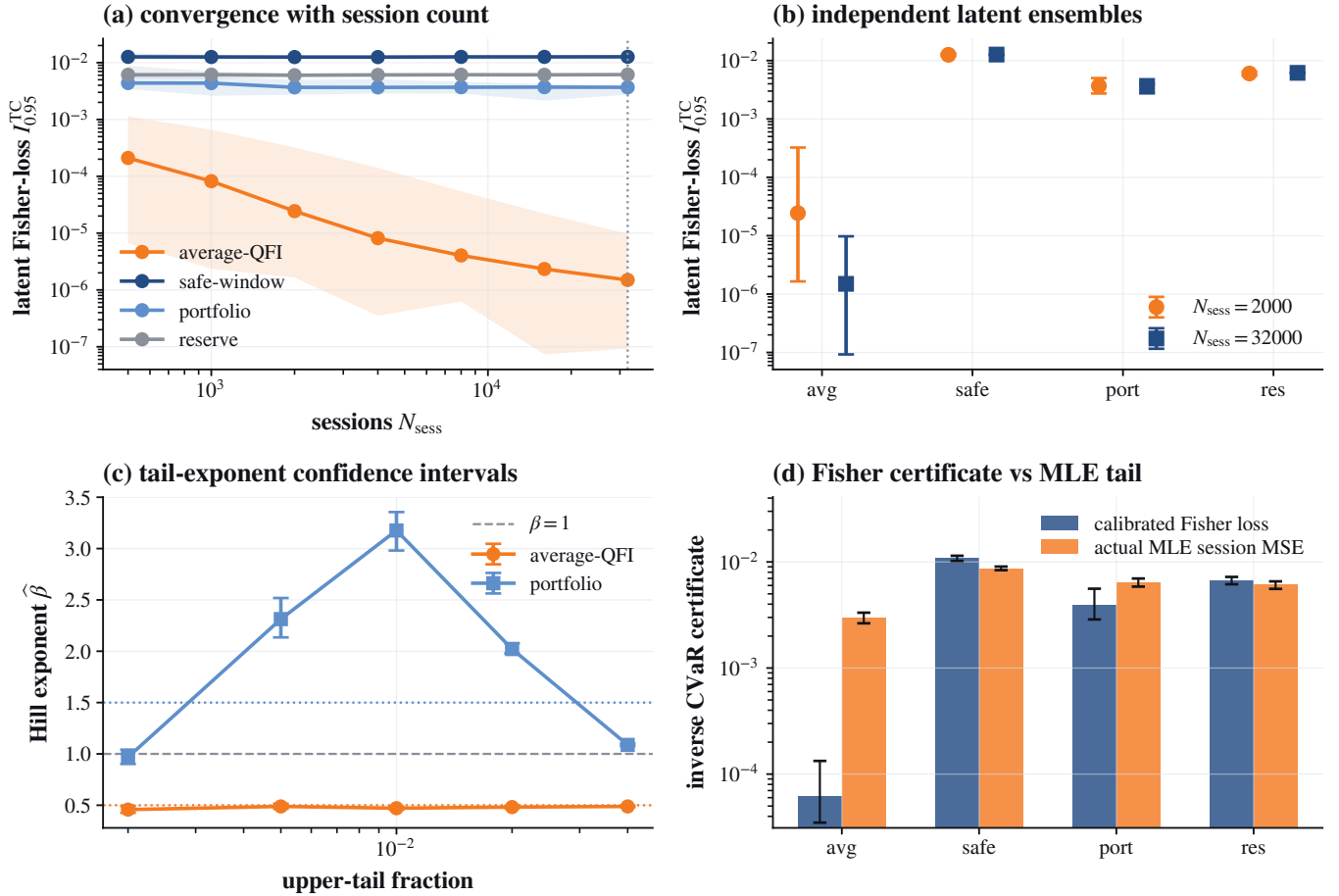


FIG. 6. **Finite-sample robustness of the shallow-NV certificate.** (a) Convergence of the latent Fisher-loss tail-certified information with session count S over 24 independent latent ensembles; bands show 10–90% seed-to-seed variation and the dotted line marks the high-stat tournament size $N_{\text{sess}} = 32000$. (b) Independent-ensemble uncertainty at $N_{\text{sess}} = 2000$ and $N_{\text{sess}} = 32000$. (c) Fixed-threshold bootstrap confidence intervals for the Hill upper-tail exponent. The average-QFI arm lies below the finite-CVaR boundary $\beta = 1$, while the portfolio steepens the finite-tail diagnostic. (d) Direct comparison between calibrated Fisher-loss inverse CVaR and actual MLE session mean-square-error (MSE) inverse CVaR, using 5000 sessions and $R_{\text{rob}} = 16$ sensing repeats per session. Error bars in (d) are session-bootstrap 90% intervals.

3. Compute $C_i(T_k) = \exp[-(T_k/T_2^*)^2] \prod_j \cos(\lambda_{ij}T_k)$.
4. Generate calibration shots at phases $\varphi = 0, \pi$. For a protocol with K interrogation times, use $n_{\text{phase}} = \max\{20, \lfloor n_{\text{cal}}/(2K) \rfloor\}$ shots for each phase at each time.
5. Estimate $\hat{C}_i(T_k) = (Y_{ik}^+/n_{\text{phase}} - Y_{ik}^-/n_{\text{phase}})/c_{\text{ro}}$, clipped to $[-1, 1]$, and $\hat{F}_i = \sum_k w_k [c_{\text{ro}} \hat{C}_i(T_k) T_k]^2$.
6. Generate sensing shots at $\varphi = \pi/2$ using the integer shot allocation above.
7. Estimate $\hat{\theta}_i$ by a one-dimensional bounded Newton MLE. The search starts at θ_0 , uses at most 12 Newton steps, clips Bernoulli probabilities to $[10^{-7}, 1 - 10^{-7}]$, and constrains the iterate to $|\theta - \theta_0| \leq \min\{0.70, 0.45\pi/\max_k T_k\}$. The update stops when the Newton step is below 10^{-8} or when the Hessian is nonfinite or smaller than 10^{-12} in

magnitude. No nuisance coordinate is fitted in the reported NV panels.

8. Store $\hat{\ell}_i = \hat{F}_{i,\theta|\mu}^{-1}$ and $(\hat{\theta}_i - \theta_0)^2$.

The calibration shot counts are therefore exact for the single-arm and reserve designs; for the three-arm portfolio the calibration uses 3996 shots because $2K \lfloor 4000/(2K) \rfloor = 3996$.

The seed protocol is deterministic. Fig. 4 uses stream 20260430 + 301 for latent sessions and calibration, and independent MLE-error streams 20260430 + 9000 + p for protocol index $p = 0, 1, 2, 3$ in the order average-QFI, safe-window, portfolio, reserve. Fig. 5 uses streams 20260430 + 1400 + $100j + r$ for the N_f sweep, 20260430 + 1500 + $100j + r$ for the coupling-range sweep, 20260430 + 1600 + $100j + r$ for the CVaR-level sweep, 20260430 + 1700 and 20260430 + 1701 for the baseline/readout-contrast calculation, 20260430 + 1800 for calibration latent con-

figurations, and $20260430 + 1900 + 100j + r$ for calibration resampling. Here j indexes the swept value and $r = 0, \dots, 23$ indexes the replicate for panels (a)–(c). Fig. 6 uses streams $20260430 + 22000 + s$ for the 24 independent convergence ensembles, $20260430 + 24000$ for Hill latent sessions, $20260430 + 24500 + 100j + \delta$ for Hill bootstraps with $\delta = 0$ for average-QFI and 50 for portfolio, $20260430 + 25000$ for the MLE-validation latent sessions, $20260430 + 26000 + p$ for MLE sensing repeats, and $20260430 + 27000 + p$ and $20260430 + 28000 + p$ for Fisher-loss and MLE-error bootstrap intervals.

The outputs are the latent average Fisher information, the empirical $\widehat{\mathcal{I}}_\alpha^{\text{TC}}$, the empirical $\widehat{\text{CVaR}}_\alpha[(\widehat{\theta} - \theta_0)^2]$, the Hill estimate $\widehat{\beta}(u)$, and the local attainability ratio $n \widehat{\text{Var}}(\widehat{\theta}) \widehat{F}$. The reported tail-certified intervals are obtained by nonparametric session-bootstrap resampling of the calibrated losses. The MLE-error survival in Fig. 4 pools R_{err} repeated sensing blocks per calibrated session. The attainability ratio is estimated by repeating the sensing block at fixed calibrated latent sessions, matching Eq. (30).

For the quasi-static sparse Ramsey model

$$F_Q(T, \xi) = T^2 C_0^2(T) \prod_{k=1}^N \cos^2(\lambda_k T), \quad (\text{Q1})$$

$$\lambda_k \sim \text{Uniform}[0, 1],$$

with $N_f = 0.05$, $\alpha = 0.9$, and $T_2^* = 5$, the average-QFI optimum is $T_{\text{avg}} = 3.5355$, while $T_{\text{safe}} = \pi/2 = 1.5708$ and the Bernoulli design formula gives $T_{\text{TC}} = 1.2030$. Controlled tail-estimation tests recover the $x^{-1/2}$ simple-zero slope, the codimension law $c/2$ for synthetic Fisher nulls, and the positive-channel cut exponent $K/2$. For a full Poisson bath with $N_f = 1$, adding a safe anchor at $T_0 = 1.2 < T_{\text{safe}}$ reduces representative extreme-loss quantiles by orders of magnitude, illustrating reserve-induced removal of the algebraic tail.

The sensitivity sweeps in Fig. 5 use the same session-resolved latent model as Fig. 4, but evaluate the calibrated Fisher-loss certificate rather than rerunning the full MLE-error survival for every point. Panels (a)–(c) use 24 independent latent ensembles with $N_{\text{sess}} = 32000$ sessions each. They plot the median safe-window/average-QFI ratio with a 90% bootstrap confidence interval for the median log-ratio; the corresponding raw 10–90% spread across finite-session ensembles is retained in `numerics/output/results.json`. Panel (d) varies c_{ro} at fixed latent ensembles. Panel (e) repeats the two-phase calibration shot model and reports the ratio between the calibration-estimated and true safe-window certificate. Panel (f) converts per-shot certificates to fixed-wall-time certificates by using

$$n_{\text{eff}} = \frac{T_{\text{wall}} - n_{\text{cal}} \langle T_k + t_{\text{dead}} \rangle_{\text{cal}}}{\langle T_k + t_{\text{dead}} \rangle_{\text{sense}}},$$

with negative values clipped to zero, and then multiplying the per-shot tail-certified information by n_{eff} . Here

T_{wall} is the per-session wall-clock budget and t_{dead} is the per-shot dead time.

The robustness checks in Fig. 6 use the baseline parameters in Table I. For panels (a) and (b), we draw 24 independent latent ensembles of size 32000 and evaluate the true latent Fisher-loss CVaR on prefixes $N_{\text{sess}} = 500, 1000, 2000, 4000, 8000, 16000, 32000$. This isolates sampling convergence from finite calibration-shot zeros; the calibrated certificate is used again in the estimator comparison. At the tournament size $N_{\text{sess}} = 32000$ and $\alpha = 0.95$, the empirical CVaR averages the largest 1600 losses; the smaller $N_{\text{sess}} = 2000$ prefix averages only 100 losses and is retained as a finite-session diagnostic. Panel (c) estimates Hill exponents from 240000 latent sessions and reports fixed-threshold bootstrap 90% intervals for upper-tail fractions 0.002–0.04. Panel (d) draws 5000 calibrated latent sessions, runs $R_{\text{rob}} = 16$ independent MLE sensing repeats per session, and compares $\widehat{\text{CVaR}}_{0.95}(\widehat{F}^{-1})$ with $\widehat{\text{CVaR}}_{0.95}[n R_{\text{rob}}^{-1} \sum_r (\widehat{\theta}_{ir} - \theta_0)^2]$ over sessions. The error bars are nonparametric session-bootstrap 90% intervals.

Appendix R: Regulator-flow proof

Let $F \geq 0$ be the session-resolved projected Fisher information and assume

$$\mathbb{P}(F < f) = A_\beta f^\beta + o(f^\beta), \quad f \downarrow 0. \quad (\text{R1})$$

Then $\ell = F^{-1}$ satisfies

$$\mathbb{P}(\ell > x) = A_\beta x^{-\beta} + o(x^{-\beta}). \quad (\text{R2})$$

For a capped loss $\ell^{\text{cap}} = \min(\ell, \ell_{\text{max}})$, the upper-tail representation of CVaR gives, for fixed $\alpha < 1$ and ℓ_{max} above the α -quantile q_α ,

$$\text{CVaR}_\alpha(\ell^{\text{cap}}) = q_\alpha + \frac{1}{1-\alpha} \int_{q_\alpha}^{\ell_{\text{max}}} \mathbb{P}(\ell > x) dx. \quad (\text{R3})$$

The finite term q_α does not affect the regulator divergence. Therefore, for $0 < \beta < 1$,

$$\text{CVaR}_\alpha(\ell^{\text{cap}}) = O(1) + \frac{A_\beta}{(1-\alpha)(1-\beta)} \ell_{\text{max}}^{1-\beta}, \quad (\text{R4})$$

while for $\beta = 1$,

$$\text{CVaR}_\alpha(\ell^{\text{cap}}) = O(1) + \frac{A_\beta}{1-\alpha} \log \ell_{\text{max}}. \quad (\text{R5})$$

This proves the hard-cap scaling.

For an additive Fisher floor $\ell_\varepsilon = (F + \varepsilon)^{-1}$, write the lower-tail measure as

$$d\mathbb{P}(F < f) = A_\beta \beta f^{\beta-1} df + o(f^{\beta-1}) df. \quad (\text{R6})$$

The divergent part of the upper-tail conditional expectation is

$$\frac{1}{1-\alpha} \int_0^{f_\alpha} \frac{A_\beta \beta f^{\beta-1}}{f + \varepsilon} df. \quad (\text{R7})$$

For $0 < \beta < 1$, set $f = \varepsilon u$. Then

$$\int_0^{f_\alpha} \frac{f^{\beta-1}}{f+\varepsilon} df = \varepsilon^{\beta-1} \int_0^{f_\alpha/\varepsilon} \frac{u^{\beta-1}}{1+u} du \sim \varepsilon^{\beta-1} \frac{\pi}{\sin(\pi\beta)}. \quad (\text{R8})$$

Hence

$$\text{CVaR}_\alpha(\ell_\varepsilon) \sim \frac{A_\beta \beta \pi}{(1-\alpha) \sin(\pi\beta)} \varepsilon^{\beta-1}. \quad (\text{R9})$$

For $\beta = 1$, the same integral gives

$$\text{CVaR}_\alpha(\ell_\varepsilon) \sim \frac{A_\beta}{1-\alpha} \log(1/\varepsilon). \quad (\text{R10})$$

If $F = Af$, then

$$(F + \varepsilon)^{-1} = A^{-1}(f + \varepsilon/A)^{-1}, \quad (\text{R11})$$

so

$$\mathcal{I}_{\alpha,\varepsilon}^{\text{TC}}(A) \propto A^\beta \varepsilon^{1-\beta} \quad (\text{R12})$$

for $0 < \beta < 1$. Thus a nonintegrable Fisher-zero tail changes the regulated scaling exponent from A to A^β .

For a finite empirical latent catalog f_1, \dots, f_N drawn from $\mathbb{P}(f < y) \sim Cy^\beta$, let $\ell_{(k)}^\downarrow$ be the k th largest inverse loss. Extreme-value order statistics give

$$\ell_{(k)}^\downarrow \asymp A^{-1} \left(\frac{CN}{k} \right)^{1/\beta}. \quad (\text{R13})$$

Averaging the largest $(1-\alpha)N$ losses gives

$$\widehat{\text{CVaR}}_\alpha(\ell) \asymp A^{-1} N^{1/\beta-1}, \quad 0 < \beta < 1, \quad (\text{R14})$$

and therefore

$$\widehat{\mathcal{I}}_{\alpha,N}^{\text{TC}} \asymp AN^{-(1-\beta)/\beta}. \quad (\text{R15})$$

At $\beta = 1$,

$$\widehat{\text{CVaR}}_\alpha(\ell) \asymp A^{-1} \log N, \quad \widehat{\mathcal{I}}_{\alpha,N}^{\text{TC}} \asymp \frac{A}{\log N}. \quad (\text{R16})$$

Finite latent catalogs therefore round, but do not remove, the Fisher-glass scaling.

DATA AND CODE AVAILABILITY

The simulation code and cached data that reproduce every main-text and supplemental figure, and every reported number, are openly available at https://github.com/E-zClap/fisher_glass_data. All results are simulation-based; no unpublished experimental data are used, and the analytic derivations are contained in the appendices. The numerical routines require only `numpy` and `matplotlib`: the shared library and figure driver is `tail_certification_numerics.py`, and the conceptual figures are built by `quenched_fisher_figures.py`. Under a fixed random seed, each figure can be redrawn from the shipped caches without rerunning the simulations (`--figures-only`) or recomputed from scratch (`--refresh-data`); exact commands are given in the repository README.

-
- [1] C. W. Helstrom, *Quantum Detection and Estimation Theory* (Academic Press, New York, 1976).
 - [2] S. L. Braunstein and C. M. Caves, “Statistical distance and the geometry of quantum states,” *Phys. Rev. Lett.* **72**, 3439 (1994).
 - [3] M. G. A. Paris, “Quantum estimation for quantum technology,” *Int. J. Quantum Inf.* **7**, 125 (2009).
 - [4] V. Giovannetti, S. Lloyd, and L. Maccone, “Quantum-enhanced measurements: Beating the standard quantum limit,” *Science* **306**, 1330 (2004).
 - [5] V. Giovannetti, S. Lloyd, and L. Maccone, “Quantum metrology,” *Phys. Rev. Lett.* **96**, 010401 (2006).
 - [6] V. Giovannetti, S. Lloyd, and L. Maccone, “Advances in quantum metrology,” *Nat. Photon.* **5**, 222 (2011).
 - [7] C. L. Degen, F. Reinhard, and P. Cappellaro, “Quantum sensing,” *Rev. Mod. Phys.* **89**, 035002 (2017).
 - [8] L. Pezzè, A. Smerzi, M. K. Oberthaler, R. Schmied, and P. Treutlein, “Quantum metrology with nonclassical states of atomic ensembles,” *Rev. Mod. Phys.* **90**, 035005 (2018).
 - [9] S. F. Huelga, C. Macchiavello, T. Pellizzari, A. K. Ekert, M. B. Plenio, and J. I. Cirac, “Improvement of frequency standards with quantum entanglement,” *Phys. Rev. Lett.* **79**, 3865 (1997).
 - [10] B. M. Escher, R. L. de Matos Filho, and L. Davidovich, “General framework for estimating the ultimate precision limit in noisy quantum-enhanced metrology,” *Nat. Phys.* **7**, 406 (2011).
 - [11] R. Demkowicz-Dobrzański, J. Kołodyński, and M. Guţă, “The elusive Heisenberg limit in quantum-enhanced metrology,” *Nat. Commun.* **3**, 1063 (2012).
 - [12] A. Smirne, J. Kołodyński, S. F. Huelga, and R. Demkowicz-Dobrzański, “Ultimate precision limits for noisy frequency estimation,” *Phys. Rev. Lett.* **116**, 120801 (2016).
 - [13] Y. Romach *et al.*, “Spectroscopy of surface-induced noise using shallow spins in diamond,” *Phys. Rev. Lett.* **114**, 017601 (2015).
 - [14] E. Paladino, Y. M. Galperin, G. Falci, and B. L. Altshuler, “ $1/f$ noise: Implications for solid-state quantum information,” *Rev. Mod. Phys.* **86**, 361 (2014).
 - [15] Y. M. Galperin, B. L. Altshuler, J. Bergli, and D. V. Shantsev, “Non-Gaussian low-frequency noise as a source of qubit decoherence,” *Phys. Rev. Lett.* **96**, 097009 (2006), doi:10.1103/PhysRevLett.96.097009.

- [16] J. Bergli, Y. M. Galperin, and B. L. Altshuler, “Decoherence in qubits due to low-frequency noise,” *New J. Phys.* **11**, 025002 (2009).
- [17] J. Bylander *et al.*, “Noise spectroscopy through dynamical decoupling with a superconducting flux qubit,” *Nat. Phys.* **7**, 565 (2011).
- [18] C. Müller, J. H. Cole, and J. Lisenfeld, “Towards understanding two-level-systems in amorphous solids: Insights from quantum circuits,” *Rep. Prog. Phys.* **82**, 124501 (2019).
- [19] J. Yoneda *et al.*, “A quantum-dot spin qubit with coherence limited by charge noise and fidelity higher than 99.9%,” *Nat. Nanotechnol.* **13**, 102 (2018).
- [20] J. B. Curtis, A. Yacoby, and E. Demler, “Non-Gaussian noise magnetometry using local spin qubits,” arXiv:2505.03877 (2025), doi:10.48550/arXiv.2505.03877.
- [21] J. Suzuki, Y. Yang, and M. Hayashi, “Quantum state estimation with nuisance parameters,” *J. Phys. A: Math. Theor.* **53**, 453001 (2020).
- [22] S. Ragy, M. Jarzyna, and R. Demkowicz-Dobrzański, “Compatibility in multiparameter quantum metrology,” *Phys. Rev. A* **94**, 052108 (2016).
- [23] M. Szczykulska, T. Baumgratz, and A. Datta, “Multiparameter quantum metrology,” *Adv. Phys. X* **1**, 621–639 (2016).
- [24] J. Zhang and J. Suzuki, “Hybrid Cramér–Rao Bound for Quantum Bayes Point Estimation with Nuisance parameters,” *Entropy* **27**, 1184 (2025), doi:10.3390/e27121184.
- [25] F. Albarelli, D. Branford, and J. Rubio, “Measurement incompatibility in Bayesian multiparameter quantum estimation,” arXiv:2511.16645 (2025), doi:10.48550/arXiv.2511.16645.
- [26] Y. Ouyang, N. Shettell, and D. Markham, “Robust Quantum Metrology With Explicit Symmetric States,” *IEEE Trans. Inf. Theory* **68**, 1809–1821 (2022), doi:10.1109/TIT.2021.3132634.
- [27] Vishnupriya K., K. J. Harikrishnan, and A. K. Pal, “Robust quantum metrology using disordered probes,” arXiv:2604.11635 (2026), doi:10.48550/arXiv.2604.11635.
- [28] J. J. Meyer, S. Khatry, D. S. Franca, J. Eisert, and P. Faist, “Quantum metrology in the finite-sample regime,” *PRX Quantum* **6**, 030336 (2025), doi:10.1103/qbnl-p6bq.
- [29] P. Artzner, F. Delbaen, J.-M. Eber, and D. Heath, “Coherent measures of risk,” *Math. Finance* **9**, 203 (1999).
- [30] R. T. Rockafellar and S. Uryasev, “Optimization of conditional value-at-risk,” *J. Risk* **2**(3), 21–41 (2000), doi:10.21314/JOR.2000.038.
- [31] R. T. Rockafellar and S. Uryasev, “Conditional value-at-risk for general loss distributions,” *J. Bank. Finance* **26**, 1443–1471 (2002), doi:10.1016/S0378-4266(02)00271-6.
- [32] T. Gorin, T. Prosen, T. H. Seligman, and M. Žnidarič, “Dynamics of Loschmidt echoes and fidelity decay,” *Phys. Rep.* **435**, 33 (2006).
- [33] H. T. Quan, Z. Song, X. F. Liu, P. Zanardi, and C. P. Sun, “Decay of Loschmidt echo enhanced by quantum criticality,” *Phys. Rev. Lett.* **96**, 140604 (2006).
- [34] M. Heyl, A. Polkovnikov, and S. Kehrein, “Dynamical quantum phase transitions in the transverse-field Ising model,” *Phys. Rev. Lett.* **110**, 135704 (2013).
- [35] M. Heyl, “Dynamical quantum phase transitions: A review,” *Rep. Prog. Phys.* **81**, 054001 (2018).
- [36] T. J. Proctor, P. A. Knott, and J. A. Dunningham, “Multiparameter estimation in networked quantum sensors,” *Phys. Rev. Lett.* **120**, 080501 (2018).
- [37] Z. Zhang and Q. Zhuang, “Distributed quantum sensing,” *Quantum Sci. Technol.* **6**, 043001 (2021).
- [38] X. Guo *et al.*, “Distributed quantum sensing in a continuous-variable entangled network,” *Nat. Phys.* **16**, 281–284 (2020), doi:10.1038/s41567-019-0743-x.
- [39] A. S. Holevo, *Probabilistic and Statistical Aspects of Quantum Theory* (North-Holland, Amsterdam, 1982).
- [40] F. Albarelli, J. F. Friel, and A. Datta, “Evaluating the Holevo Cramér–Rao bound for multiparameter quantum metrology,” *Phys. Rev. Lett.* **123**, 200503 (2019), doi:10.1103/PhysRevLett.123.200503.
- [41] Y. Yang, G. Chiribella, and M. Hayashi, “Attaining the ultimate precision limit in quantum state estimation,” *Commun. Math. Phys.* **368**, 223 (2019).
- [42] P. Zanardi and N. Paunković, “Ground state overlap and quantum phase transitions,” *Phys. Rev. E* **74**, 031123 (2006).
- [43] P. Zanardi, M. G. A. Paris, and L. Campos Venuti, “Quantum criticality as a resource for quantum estimation,” *Phys. Rev. A* **78**, 042105 (2008).
- [44] I. Frérét and T. Roscilde, “Quantum critical metrology,” *Phys. Rev. Lett.* **121**, 020402 (2018).
- [45] M. M. Rams, P. Sierant, O. Dutta, P. Horodecki, and J. Zakrzewski, “At the limits of criticality-based quantum metrology: Apparent super-Heisenberg scaling revisited,” *Phys. Rev. X* **8**, 021022 (2018), doi:10.1103/PhysRevX.8.021022.
- [46] L. Garbe, M. Bina, A. Keller, M. G. A. Paris, and S. Felicetti, “Critical quantum metrology with a finite-component quantum phase transition,” *Phys. Rev. Lett.* **124**, 120504 (2020).
- [47] E. M. Kessler, I. Lovchinsky, A. O. Sushkov, and M. D. Lukin, “Quantum error correction for metrology,” *Phys. Rev. Lett.* **112**, 150802 (2014).
- [48] W. Dür, M. Skotiniotis, F. Fröwis, and B. Kraus, “Improved quantum metrology using quantum error correction,” *Phys. Rev. Lett.* **112**, 080801 (2014).
- [49] G. Arrad, Y. Vinkler, D. Aharonov, and A. Retzker, “Increasing sensing resolution with error correction,” *Phys. Rev. Lett.* **112**, 150801 (2014).
- [50] P. Sekatski, M. Skotiniotis, J. Kołodyński, and W. Dür, “Quantum metrology with full and fast quantum control,” *Quantum* **1**, 27 (2017).
- [51] M. M. Rams and B. Damski, “Quantum fidelity in the thermodynamic limit,” *Phys. Rev. Lett.* **106**, 055701 (2011).
- [52] A. B. Harris, “Effect of random defects on the critical behaviour of Ising models,” *J. Phys. C: Solid State Phys.* **7**, 1671 (1974).
- [53] E. L. Hahn, “Spin echoes,” *Phys. Rev.* **80**, 580 (1950).
- [54] L. Viola, E. Knill, and S. Lloyd, “Dynamical decoupling of open quantum systems,” *Phys. Rev. Lett.* **82**, 2417 (1999).
- [55] M. J. Biercuk *et al.*, “Optimized dynamical decoupling in a model quantum memory,” *Nature* **458**, 996 (2009).
- [56] G. de Lange, Z. H. Wang, D. Ristè, V. V. Dobrovitski, and R. Hanson, “Universal dynamical decoupling of a single solid-state spin from a spin bath,” *Science* **330**, 60 (2010).
- [57] J. M. Taylor *et al.*, “High-sensitivity diamond magnetometer with nanoscale resolution,” *Nat. Phys.* **4**, 810

- (2008).
- [58] H. J. Mamin, M. Kim, M. H. Sherwood, C. T. Rettner, K. Ohno, D. D. Awschalom, and D. Rugar, “Nanoscale nuclear magnetic resonance with a nitrogen-vacancy spin sensor,” *Science* **339**, 557 (2013).
- [59] T. Staudacher *et al.*, “Nuclear magnetic resonance spectroscopy on a (5-nanometer)³ sample volume,” *Science* **339**, 561 (2013).
- [60] F. Casola, T. van der Sar, and A. Yacoby, “Probing condensed matter physics with magnetometry based on nitrogen-vacancy centres in diamond,” *Nat. Rev. Mater.* **3**, 17088 (2018).
- [61] J. Rovny, S. Gopalakrishnan, A. C. Bleszynski Jayich, P. Maletinsky, E. Demler, and N. P. de Leon, “Nanoscale diamond quantum sensors for many-body physics,” *Nat. Rev. Phys.* **6**, 753–768 (2024), doi:10.1038/s42254-024-00775-4.
- [62] B. M. Hill, “A simple general approach to inference about the tail of a distribution,” *Ann. Stat.* **3**, 1163 (1975).
- [63] P. Embrechts, C. Klüppelberg, and T. Mikosch, *Modelling Extremal Events for Insurance and Finance* (Springer, Berlin, 1997).
- [64] L. de Haan and A. Ferreira, *Extreme Value Theory: An Introduction* (Springer, New York, 2006).